Materials Science & Engineering A 878 (2023) 145180

Contents lists available at ScienceDirect

Materials Science & Engineering A

journal homepage: www.elsevier.com/locate/msea

Effect of austenite fraction and stability on strength-hardening-ductility in additively manufactured 17-4 PH stainless steel containing nitrogen

Saadi A. Habib [a,*], Steven P. Mates [a], Fan Zhang [a], Mark R. Stoudt [a], James S. Zuback [a], Olaf Borkiewicz [b]

[a] National Institute of Standards and Technology, Gaithersburg, Maryland, USA
[b] X-ray Science Division, Advanced Photon Source, Argonne National Laboratory, Argonne, Illinois, USA

ARTICLE INFO

Keywords:
Nitrogen
Austenite
Martensite
DIMT
TRIP
Transformation
HEXRD

ABSTRACT

Additively-manufactured (AM) 17-4 precipitation-hardening (PH) martensitic stainless steel (SS) built from nitrogen-atomized powder often retains a large volume fraction of austenite. The retained austenite lowers the yield strength compared to both wrought and AM 17-4 SS built from argon-atomized powder, hindering its use in many applications. However, retained austenite allows for high work hardening and high ductility through deformation-induced martensitic transformation (DIMT). This work systematically investigates the influence of various heat treatments on the volume fraction and stability of the retained austenite from tensile loading in AM 17-4 SS containing a mass fraction of 0.13% nitrogen (AM 17-4N SS). Synchrotron-based high-energy x-ray diffraction (HEXRD) is used to quantify the austenite volume fraction resulting from the heat treatments and the extent of DIMT in tensile specimens loaded to various plastic strains and specimens loaded to fracture. We show that by altering the volume fraction and stability of the retained austenite in AM 17-4N SS using different heat treatments, the DIMT process can be utilized to vary the strength, work hardening, and ductility, thus enabling its use in a wide range of applications. The AM 17-4N SS is also shown to meet or exceed the peak aged requirements for wrought 17-4 SS with yield strength (YS) of >1200 MPa, an ultimate tensile strength (UTS) of >1500 MPa, and a uniform elongation of ≥13% while retaining ≈ 20% volume fraction of austenite.

1. Introduction

Additive manufacturing (AM) of metals has enabled the fabrication of complex parts with intricate features. Among the many materials used for AM, martensitic precipitation-hardenable (PH) 17-4 stainless steel (SS) (UNS S17400 or Type 630 SS) is of interest for its weldability, strength, wear resistance, and corrosion resistance properties [1]. Hardenability of 17-4 SS arises from the formation of nanometer-sized Cu-rich precipitates in the martensite during age-hardening [2–7]. While peak age-hardening of 17-4 SS results in high yield strength compared to many other stainless steels, it also exhibits a lower work hardening and a lower uniform elongation. In order to improve the work hardening and ductility, an over-aging treatment is necessary, but at the cost of strength [2–5,7–11], often referred to as the strength-ductility tradeoff.

Additively manufactured 17-4 SS (AM 17-4 SS) is typically produced from feedstocks of either argon- or nitrogen-atomized powder. Nitrogen-atomized powder is preferable for AM builds due to the lower cost. Additionally, nitrogen is soluble in steel; therefore, nitrogen-atomized powder contains fewer hollow powder particles compared to argon-atomized powder [12–14]. This is favorable since the hollow particles can become porosity in the AM material, reducing its ductility [12]. An additional advantage is that nitrogen has been shown to improve the corrosion resistance of 17-4 SS [15,16]. However, like carbon, nitrogen is an effective austenite stabilizer in steel [17,18]. This is problematic because the martensite start and martensite finish temperatures for wrought 17-4 SS are approximately 132 °C and 32 °C, respectively [1]. As such, the presence of nitrogen reduces the martensite start temperature resulting in a large volume fraction of retained austenite at room temperature. It has been shown that AM 17-4 SS material built using nitrogen-atomized powder containing a mass fraction of ≥ 0.1% nitrogen can contain up to 100% retained austenite in the as-built condition [19–24]. AM 17-4 SS containing a mass fraction of ≥ 0.1% nitrogen will be referred to as AM 17-4N SS, similar to the naming convention of 316

* Corresponding author.
E-mail address: saadi.habib@nist.gov (S.A. Habib).

https://doi.org/10.1016/j.msea.2023.145180
Received 3 January 2023; Received in revised form 14 May 2023; Accepted 16 May 2023
Available online 18 May 2023
0921-5093/Published by Elsevier B.V.

N SS [25], to distinguish it from conventional wrought and cast 17-4 SS that typically contain a mass fraction of ≤0.05% nitrogen [26].

The AM process also causes a complex solidification microstructure, elemental segregation, and the formation of Cu-rich precipitates in the as-built condition [27–29]. A post-build homogenization/solutionization heat treatment is often necessary to homogenize the material and dissolve the Cu-rich precipitates to gain the maximum age-hardening potential during the subsequent age-hardening heat treatment. The solutionization treatment also decreases the carbon and nitrogen content in the matrix by forming Nb(C,N) precipitates, which increases the martensite start temperature [27,28]. Lass *et al.* [27] have taken advantage of this with the assistance of a sub-room temperature treatment to decrease the volume fraction of austenite in AM 17-4N SS and they were successful at achieving 95% volume fraction of martensite. Others have attempted to enhance the mechanical properties of AM 17-4N SS with large volume fraction of retained austenite by altering the austenitization heat treatment and age-hardening protocol compared to wrought [22,30]. However, the low yield stress and high work hardening persist at low strains, but with high ultimate tensile strength (UTS) and uniform elongation.

It is well known that retained austenite in steel can significantly improve work hardening and ductility through deformation-induced martensitic transformation (DIMT) [31,32], such as in transformation-induced plasticity (TRIP) steel [33,34], quenched and partitioned (Q&P) steel [35–37], medium-manganese steel [38], and austenitic stainless steels [39–42]. The DIMT behavior typically depends on the chemical composition, microstructure, and morphology of the austenite and martensite phases, and the loading conditions (i.e., temperature, stress state, and strain rate) [31,32,34,36,37,40,43,44]. Although DIMT can improve the work hardening and ductility, a high austenite volume fraction and a low austenite stability can result in unfavorable properties. For example, Facchini *et al.* [21] reported a volume fraction of 72% retained austenite in AM 17-4N SS, which resulted in low yield stress, large discontinuous yielding (Lüders banding), and high work hardening, leading to high ductility. Also, Phan *et al.* [45] reported that austenite is unstable in AM 17-4N SS such that ≈ 80% of the retained austenite transforms to martensite by 3% plastic strain. In conventional DIMT steels, the austenite fraction and stability are specifically tailored to achieve a high strength and to promote a gradual DIMT as the material is deformed, resulting in work hardening that is distributed over large strain and high uniform ductility. Furthermore, while retained austenite can enhance the ductility and work hardening behavior of 17-4 SS, it also limits the age-hardening potential if a large volume fraction of austenite is retained because of the solubility of Cu in austenite [46]. Therefore, while retained austenite in AM 17-4 SS can seem beneficial, high volume fractions of austenite and the lack of austenite stability are unfavorable if the stress and ductility are to be optimized in AM 17-4N SS.

The majority of the literature on AM 17-4 SS have focused on eliminating the retained austenite and obtaining wrought properties by utilizing argon-atomized powder, and/or post build heat treatments [22,23,27,28,30,42,46–63]. To date, it is not well understood the impact of retained austenite on the mechanical properties of AM 17-4N SS especially after age-hardening heat treatment. Therefore, in this work, we investigate the effect of retained austenite on the mechanical properties of AM 17-4N SS by utilizing different starting heat treatments to vary the austinite fraction. Additionally, a peak age-hardening (H900) heat treatment was performed to the above conditions specifically to increase the strength of the material without over-aging since the ductility improvement will arise from the DIMT process.

2. Material and experimental procedures

2.1. Material and AM process

AM 17-4N SS was built at the National Institute of Standards and Technology (NIST) using virgin, nitrogen-atomized powder (EOS GP1[1] Lot number F211601) on an EOS M290 commercial powder bed fusion machine. The relevant build parameters are shown in Table 1. The material was built as solid towers and numbered as shown in Fig. 1a. A comparative study was also performed on commercially available 1.5 mm thick wrought sheet of 17-4 SS in the as-received solutionized condition (*Wr-CondA*). The chemical composition of the AM and wrought materials are reported in Table 2 and both materials conform to ASTM A564 and ASTM A693 standards [6,64], although the nitrogen limits were never stated within both standards.

2.2. Heat treatments and computational thermodynamics

The AM build was stress-relieved at 650 °C for 1 h (at temperature) followed by a furnace cool prior to being machined off the build plate using wire electrical discharge machining (EDM). The stress-relieved (SR) material will be referred to as *AM-SR*. However, a solidification microstructure and elemental segregation are developed during the AM process and during the stress-relief heat treatment. As such, a post-build homogenization heat treatment was performed prior to the precipitation hardening (aging) treatment.

Cheruvathur *et al.* [28] recommended a homogenization at 1150 °C to alleviate micro segregation and recrystallize the microstructure on a similar nitrogen-atomized AM 17-4N SS, which was based on AMS-5355 [26]. To insure a 1150 °C homogenization heat treatment was sufficient to homogenize the AM material used in this study, phase fractions of the equilibrium phases as a function of temperature were computed using Thermo-Calc version 2022a with the TCFe10 database for the composition listed in Table 2 and results are shown in Fig. 2. The elements O, S, P and Si were not included in the simulation for simplicity. A homogenization at 1150 °C was sufficient since the only 2 stable phases predicted are face-centered cubic (FCC) austenite and Nb(C,N). Therefore, Tower #3, Tower #4, and Tower #5 (shown in Fig. 1a) were encapsulated in quartz ampules under vacuum and then first homogenized at 1150 °C for 1 h (at temperature) and air cooled, and then second austenitized at 1050 °C for 1 h (at temperature) and air cooled without removing the material from the quartz ampules. The cooling rate of the material within the quartz ampules were not recorded, but it was slower than air cooling without encapsulation and has likly influenced the microstructure [65]. The additional austenization was performed at 1050 °C to further reduce the nitrogen content in the matrix by forming and growing additional Nb(C,N), and to potentially refine the prior austenite grain size [1,62]. The homogenized and austenitized AM material will be referred to as *AM-HA*. After the HA heat treatments,

Table 1
AM build parameters. The standard EOS gas flow nozzle was used.

Parameter	Value
Laser Power	220 W
Beam Diameter	80 μm
Scan Speed	755.5 mm/s
Hatch Spacing	100 μm
Stripe Width	12 mm
Layer Thickness	40 μm
Scan direction	+67°/layer
Atmosphere	N_2
Build Platform Temperature	80 °C

[1] Certain commercial equipment, instruments, or materials are identified in this paper to elucidate the experimental procedure. Such identifications are not intended to imply recommendation or endorsement by the National Institute of Standards and Technology, nor are they intended to imply that the materials or equipment identified are necessarily the best available for the purpose.

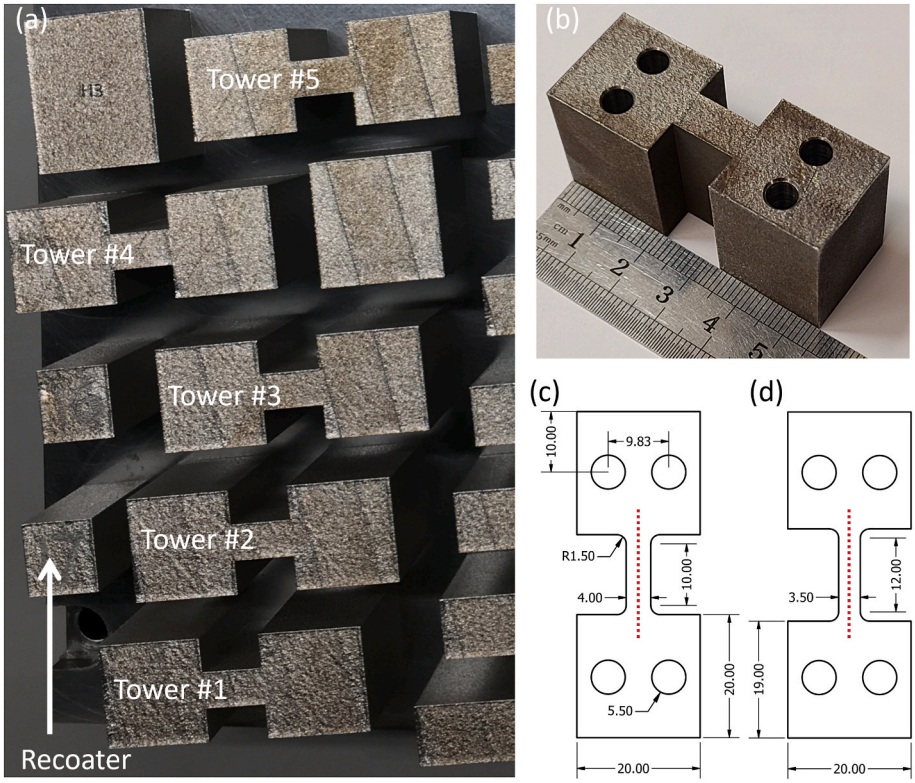

Fig. 1. (a) As-built towers on the build plate, (b) a single tower once removed off the build plate, (c) final specimen dimensions (in mm) for the AM-SR and AM-SR+H900 conditions, and (d) final specimen dimensions (in mm) for the AM-HA, AM-HA+H900, AM-HAQ, AM-HAQ+H900, Wr-CondA, and Wr-H900 conditions. The red dotted line in (c) and (d) are location of the HEXRD line scan (see Section 2.6 for experimental procedures). A virtual DIC extensometer with an 8 mm gauge length and a 10 mm gauge length were used for the engineering strain calculation for specimen (c) and (d), respectively. (For interpretation of the references to color in this figure legend, the reader is referred to the Web version of this article.)

Table 2
The chemical composition of the AM 17-4N SS (powder and solid built material) and wrought 17-4 SS sheet. The powder composition was provided from manufacturer (EOS GP1, Lot number F211601).

Element	AM – Powder	AM – Solid	Wrought
	Mass fraction [%]	Mass fraction [%]	Mass fraction [%]
Cr	15.8	16.9	15.4
Ni	4.4	4.77	4.73
Cu	3.9	4.67	3.32
Nb	0.23	0.22	0.26
Mn	0.4	0.40	0.51
Mo	0.1	0.078	0.23
C	0.05	0.04	0.04
N	N/A	0.13	0.029
O	N/A	0.033	0.01
P	0.03	0.007	0.001
Si	0.6	0.59	0.21
S	<0.01	0.004	0.001
Fe	Bal.	Bal.	Bal.

Tower #5 was removed from encapsulation and then placed in liquid nitrogen for 30 min. This condition will be referred to as *AM-HAQ*. The liquid nitrogen treatment was used to reduce the austenite fraction in the AM-HA condition since the martensite end temperature is below room temperature. This provides two different conditions with different austenite volume fractions, in addition to the AM-SR condition.

Aging treatment at 482 °C ± 8 °C for 1 h (referred to as H900, the same as the wrought naming convention [1,6,66]) were also performed to the AM-SR, AM-HA and AM-HAQ starting conditions. These conditions will be referred to as *AM-SR+H900, AM-HA+H900* and *AM-HAQ+H900*. An H900 heat treatment was also performed for the wrought 17-4 SS (Wr-H900) as a comparison to the AM material. A summary of the heat treatments for the AM and wrought materials investigated are shown in Table 3.

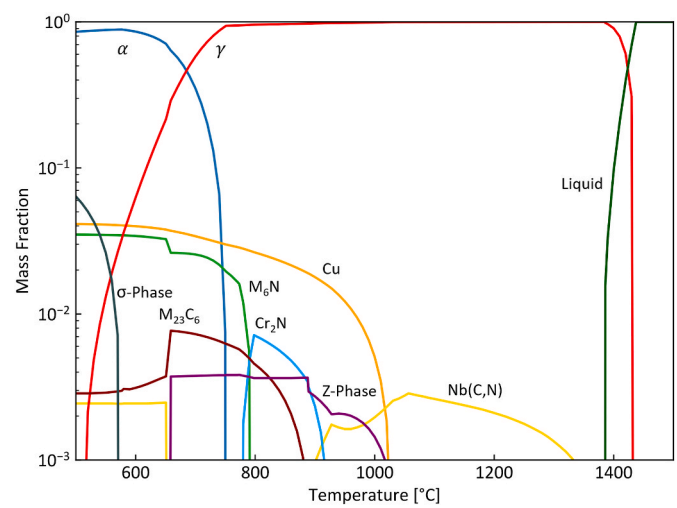

Fig. 2. Phase fractions of the equilibrium phases as a function of temperature for the AM 17-4N SS.

2.3. Microscopy measurements

Samples were cut from the tab sections of undeformed tensile bars for microscopic analysis. The specimens were mounted in a conductive phenolic resin and polished according to standard metallographic practice. A final polishing step using a vibratory polishing system with non-agglomerating 0.2 μm colloidal silica for scanning electron microscopy (SEM), electron backscatter diffraction (EBSD) and energy dispersive x-ray spectroscopy (EDS) measurements. EDS maps of the composition were acquired using a 15 KeV accelerating voltage, a 500 pA probe current, and a 10 mm working distance. Similarly, EBSD phase and grain orientation maps were acquired using a 20 KeV voltage, a 4 nA probe current, a nominal working distance of 20 mm, and a 0.5 μm step

Table 3
Heat treatments for AM 17-4N SS and wrought 17-4 SS. The heat treatments were performed in order from left to right. The stress-relieved heat treatment was furnace cooled, and the homogenized and austenitized heat treatments were air-cooled within encapsulation/vacuum. The tower and specimen geometry for each condition is also show for each condition.

Material- Condition	AM Tower/Specimen Geometry	Stress-Relieved	Homogenized	Austenitized	Cryogenic	Aged
AM-SR	#1 & #2/Fig. 1c	650 °C 1 h				
AM-SR+H900	#1 & #2/Fig. 1c	650 °C 1 h				482 °C 1 h
AM-HA	#3 & #4/Fig. 1d	650 °C 1 h	1150 °C 1 h	1050 °C 1 h		
AM-HA+H900	#3 & #4/Fig. 1d	650 °C 1 h	1150 °C 1 h	1050 °C 1 h		482 °C 1 h
AM-HAQ	#5/Fig. 1d	650 °C 1 h	1150 °C 1 h	1050 °C 1 h	−196 °C 30 min	
AM-HAQ+H900	#5/Fig. 1d	650 °C 1 h	1150 °C 1 h	1050 °C 1 h	−196 °C 30 min	482 °C 1 h
Wr-CondA	NA/Fig. 1d			As-Received		
Wr-H900	NA/Fig. 1d			As-Received		482 °C 1 h

size. The EBSD data were post processed using MTEX [67].

2.4. Hardness measurements

Samples from undeformed material were mounted in glass-filled phenolic, ground, and polished to a 1 μm finish, and lightly etched with Marble's reagent prior to hardness measurements. The microhardness of each sample was measured using an instrumented hardness machine equipped with a Vickers indenter. For each indentation, the indenter tip approached the sample at 50 μm/min until a contact force of 25 mN was reached. A load was then applied at 98 N/min until the target load of 4.9 N was obtained. The indenter maintained the maximum load of 4.9 N for 5 s, at which point the sample was unloaded at 40 N/min. A total of 9 indents were made in each sample, arranged in a 3 indent by 3 indent square grid with a 250 μm spacing about the sample center. The Vickers hardness was calculated according to ASTM E92 [68], and each reported value represents the average and standard deviation of 9 individual indents.

2.5. Quasi-static tension experiments

Quasi-static tension experiments were performed on all the conditions described in Table 3. Tower #1 and Tower #2 with the AM-SR heat treatment were initially wire EDM machined to the outside profile shown in Fig. 1c, and then machined into 1.5 mm thick tensile specimens using wire EDM. Similarly, once the HA and HAQ heat treatments were performed on the Tower #3, Tower #4, and Tower #5, the outside profile dimensions for the tensile specimens were machined using computer-numerical-control (CNC) milling to the dimensions shown in Fig. 1d, after which 1.5 mm thick specimens were machined using wire EDM. Tension experiments were also performed on identically shaped wrought 17-4 SS sheet samples (1.5 mm thick) in the rolling direction in the as-received austenitized condition (*Wr-CondA*) and H900 condition (*Wr-H900*) to compare with the various AM material conditions. These specimens were initially waterjet machined oversized and then CNC milled to the dimensions shown in Fig. 1d. The length/width ratio was increased for the AM-HA and AM-HAQ conditions (from Fig. 1c to d) for a better representation of engineering strain due to the heterogenous deformation shown later in Fig. 10.

The quasi-static tension experiments were performed using a servo-hydraulic load frame with a 50 kN load cell at a constant velocity of 0.00375 mm/s for the specimen shape as in Figs. 1c and 0.00438 mm/s for the specimen shape as in Fig. 1d to achieve a common nominal strain rate of 3×10^{-4} s^{-1}. Stereo digital image correlation (DIC) was used to calculate the surface strains of the samples. Two Point Gray 12 MP cameras (GS3-U3-123S6M) with Tokina AT-X Pro Macro 100 F2.8 lenses were used for the DIC measurements with a stereo-angle of ≈ 22.5°, resulting in an average magnification of 5.2 μm/pixel. The images and data were acquired at 0.5 Hz with a 6 ms exposure. Correlated Solutions Vic3D was used for the DIC calculations. The subset size, step size, and filter size of 25 pixels, 8 pixels, and 5 pixels were used for the DIC analysis, respectively, which corresponded to a 0.3 mm virtual strain gauge (VSG) size following the procedures by Ref. [69]. Average strain noise floor, represented by the spatial standard deviation, were 266 μm/m and 247 μm/m for ε_{xx} and ε_{yy}, respectively. An 8 mm and 10 mm gauge length virtual extensometer was used to calculate the engineering strain for the stress-strain curves for specimen geometries in Fig. 1c and Fig. 1d, respectively, due to the slight difference in specimen geometry between AM-SR(+H900) conditions and all other conditions. Note, this makes comparing the results beyond UTS between the two geometries not straightforward. The fracture strain for each experiment was reported based on the engineering gauge length strain on the last DIC frame before fracture. In addition to the gauge length strain, the local von-Mises effective strain within the neck was reported as

$$\bar{\varepsilon} = \frac{2}{\sqrt{3}}\sqrt{\varepsilon_1^2 + \varepsilon_1\varepsilon_2 + \varepsilon_2^2}, \tag{1}$$

where ε_1 and ε_2 are the true local DIC principal surface strains from the Hencky strain tensor and assuming incompressibility using an average of a 0.5 mm diameter area within the neck up to the last DIC frame before fracture. The 0.2% offset yield stress (YS), engineering ultimate tensile strength (UTS), and engineering strain at UTS (uniform elongation) were calculated following the procedures in ASTM E8 [70].

2.6. HEXRD measurements

High-energy X-ray diffraction (HEXRD) measurements were performed at 11-ID-B of the Advanced Photon Source, Argonne National Laboratory, to determine the present phases and their fractions. The X-ray energy was 86.7 keV, corresponding to an X-ray wavelength of 0.143 Å. The X-ray flux density was ≈ 10^{13} photon · mm^{-2} · s^{-1}. A Perkin-Elmer 1621 a-Si 2D area detector was used with a sample to detector distance of 1000 mm to acquire the XRD data in transmission mode. This setup covered a diffraction q range between ≈ 1.5 Å^{-1} and ≈ 8.5 Å^{-1}. Here, $q = 2\pi/\lambda \cdot \sin(\theta)$, where θ is one-half of the diffraction angle 2θ and λ is the X-ray wavelength. A beam of 200 μm × 200 μm was used to perform spatially resolved measurements along the gauge length of the specimens with a step size of 200 μm, as illustrated in Fig. 1c and d. The measurements were performed on the undeformed tensile specimens, and on specimens loaded to various strains and then unloaded (interrupted experiments) for ex-situ HEXRD measurements. The measurements were calibrated using NIST-traceable CeO_2 SRM 674b and the data were reduced within GSAS-II program. These types of spatially resolved HEXRD measurements are sensitive to the phase-fraction heterogeneity in the material containing multiple phases [71]. The analysis was performed following the procedures described in Ref. [24]. Note, martensite is a body centered tetragonal (BCT) crystal structure, but the c/a lattice parameter ratio is close to 1 such that it is undistinguishable from a body-centered cubic (BCC) crystal structure in 17-4 SS. As such, BCC crystal structure is used to refer to the martensite when discussing the HEXRD results.

3. Results

3.1. Initial microstructure

EBSD maps of the Wr-H900 and AM-HA+H900 material are shown in Fig. 3. Qualitatively, the average prior austenite grain size of the wrought material is smaller than the AM-HA condition. This is a result of the wrought material being thermo-mechanically processed, producing a fine grain structure. The EDS maps for the Nb, N, Si, O, and Cu for the Wr-H900, AM-SR, and AM-HA conditions are shown in Fig. 4. The AM-SR condition does not exhibit any evidence of elemental segregation at the measured length scale. For the AM-HA condition, Nb-rich precipitates are present, likely Nb(C,N) and possibly Z-Phase, which are rich in Nb, Cr, N, and C. The Wr-H900 sample also show Nb-rich precipitates, but they are finer than the AM-HA material. The Nb content in both AM and wrought materials are similar, therefore the retained nitrogen content in solid solution in the AM material is limited by the Nb content, which is typically 5 times that of carbon in wrought material [72]. EDS maps of Cr and Ni are not shown because they do not show any segregation, but they are depleted at some of the larger Nb-rich precipitates. Additionally, there are no noteworthy segregation or depletion in the EDS maps of Mn. Regardless, the EDS results showed precipitates rich in Si and O in the AM-HA material, which are not present in the wrought material. The AM 17-4N composition contained approximately 3 times the Si content of wrought 17-4 SS. Si is typically added for its high oxygen affinity [73], which is important in AM material due to the higher oxygen content from the atomization of the powder and AM process. Some Nb-rich precipitates are adjacent to the precipitates rich in Si and O. While the nanometer-scale Cu-rich precipitates responsible for age-hardening to the H900 condition cannot be resolved by EDS at this resolution, large Cu-rich precipitates are present in all samples tested except the AM-SR sample. Finally, many of the Nb-rich, Si + O rich, and Cu-rich precipitates in the AM-HA condition seem to be located along the prior austenite grain boundaries.

Box plots of FCC volume fraction for the undeformed tensile specimen for the AM-SR, AM-HA, AM-HA+H900, AM-HAQ and AM-HAQ+H900 conditions are shown in Fig. 5a. The measurements are obtained from 100 individual HEXRD measurement points (200 μm × 200 μm beam area through the 1.5 mm thick specimen) measured 200 μm apart along the gauge length of the specimens as shown in Fig. 1c and d. Average FCC volume fraction values for each material condition are listed in Table 4. There is large variation in the FCC volume fraction along the length of the undeformed sample for all heat treatments, indicating microstructural heterogeneity, or the lack of illuminated grains within the HEXRD measurement volume and potentially crystallographic texture effects [74,75]. The variation does not seem to be influenced by the difference in cross sectional area of the as-built towers between the tab ends and gauge section based on the HEXRD data along the length of the sample. The AM-SR condition has an average FCC volume fraction of 0.390 ± 0.029 (± 1σ for all reported uncertainties), which is significantly lower than the expected as-built FCC volume fraction of 1.0. The AM-HA and AM-HA+H900 conditions have similar FCC volume fractions of 0.266 ± 0.062 and 0.264 ± 0.059, respectively. The average FCC volume fraction is 0.198 ± 0.044 for the AM-HAQ condition, which is 0.069 less than the AM-HA condition. The average FCC volume fraction slightly increases to 0.224 ± 0.054 for the AM-HAQ+H900 condition although it is within 1σ of the measurements. If true, this could indicate the possibility of reverted austenite, which is often associated with elemental diffusion of austenite stabilizers from the martensite to the austenite [9–11].

Box plots of FCC lattice parameters and BCC lattice parameters for the undeformed tensile specimen for the AM-SR, AM-HA, AM-HA+H900, AM-HAQ and AM-HAQ+H900 conditions are shown in Fig. 5b and c. The average BCC and FCC lattice parameter of the undeformed tensile specimen for the different material conditions are summarized in Table 4. The average FCC lattice parameters are higher in the aged conditions for both AM-HA and AM-HAQ conditions. The FCC lattice parameter for the AM-SR is the highest at 3.5982 Å ± 0.0006 Å. Conversely, the average BCC lattice parameters are lower in the aged conditions for both AM-HA and AM-HAQ conditions. The BCC lattice parameter for the AM-SR is similar to the unaged AM-HA and AM-HAQ conditions. This indicates tempering potential for the AM-SR condition, although the HEXRD measurements on the AM-SR+H900 condition were not performed.

3.2. Mechanical behavior

3.2.1. Hardness

The AM-SR condition has a hardness of 438 HV ± 12 HV and the hardness decreases to 383 HV ± 6 HV after the HA heat treatment. The liquid nitrogen treatment (AM-HAQ condition) increased the hardness to 404 HV ± 7 HV as expected since it decreased the austenite fraction. After aging to H900, the hardness increases for both the AM-HA+H900 and AM-HAQ+H900 conditions to 482 HV ± 12 HV and 467 HV ± 8 HV, respectively. The average hardness for the AM-HA+H900 condition is higher, although statistically insignificant. Note, the mechanical polishing used to prepare the samples has been shown to promote martensite transformation at the surface [24], which may increase the measurable hardness.

3.2.2. Tensile behavior

Tensile stress-strain curves for the different wrought 17-4 SS and AM 17-4N SS conditions are shown in Fig. 6. The figure also shows the interrupted experiments for the ex-situ HEXRD measurements used to determine the extent of DIMT that occurs with different amounts of plastic strain. The corresponding average elastic modulus, YS, UTS, uniform elongation, local principal strain ε_1 and ε_2, and $\bar{\varepsilon}$ prior to fracture are summarized in Table 5. A summary of the experiments is

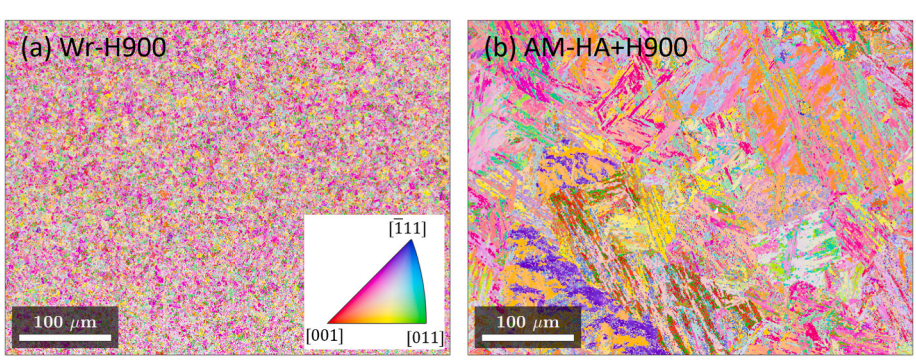

Fig. 3. EBSD distribution maps of the (a) Wr-H900 and (b) AM-HA+H900 conditions. The z-axis (out of plane) represents the normal direction to the sheet and the build direction for the wrought and AM conditions, respectively. The inverse pole figure orientation map for ferrite is oriented in the z-axis.

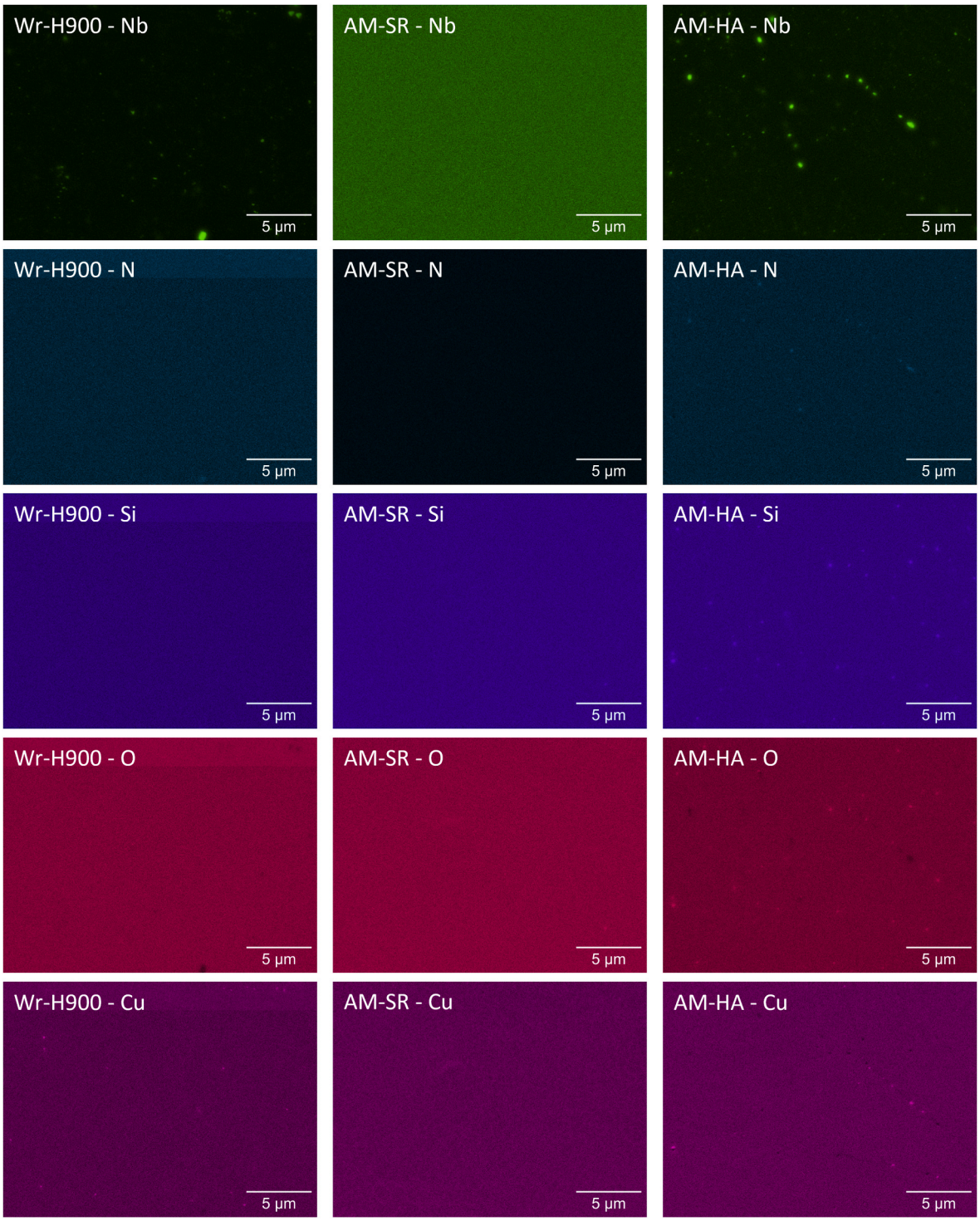

Fig. 4. EDS maps for Nb, N, Si, O, and Cu for Wr-H900, AM-SR, and AM-HA conditions.

reported in Fig. 7. The true stress-strain curves up to the UTS and the corresponding true strain hardening versus true strain for all the wrought 17-4 and AM 17-4N conditions are shown in Fig. 8. Wr-CondA exhibits a low YS of 1074 MPa, consistent with literature results [1,76], and a low uniform strain (0.020 m/m). Aging the Wr-CondA material to H900 (Wr-H900) increases the YS approximately 300 MPa as shown in Fig. 6a. The gauge length strain at fracture is between 15% and 19% engineering strain, but locally reaches up to 100% true effective strain prior to final fracture. This indicates the wrought material cannot accommodate sufficient work hardening to achieve high uniform elongation, but it is ductile within the neck.

The YS of AM-SR is low compared to wrought, at 484 MPa ± 42 MPa, but significant hardening is present up to the UTS of 1543 MPa ± 7 MPa as shown in Fig. 6b and Table 5. There is large scatter in the mechanical response between the AM-SR samples, indicative of the material variability. The AM-SR condition exhibits good ductility, with uniform elongation of >0.09 m/m. The YS of the AM-HA condition did not increase significantly compared to the AM-SR condition, but the UTS reduced (see Fig. 6c). However, liquid nitrogen treatment in the AM-HAQ condition increased the YS to 694 MPa ± 4 MPa (Fig. 6d),

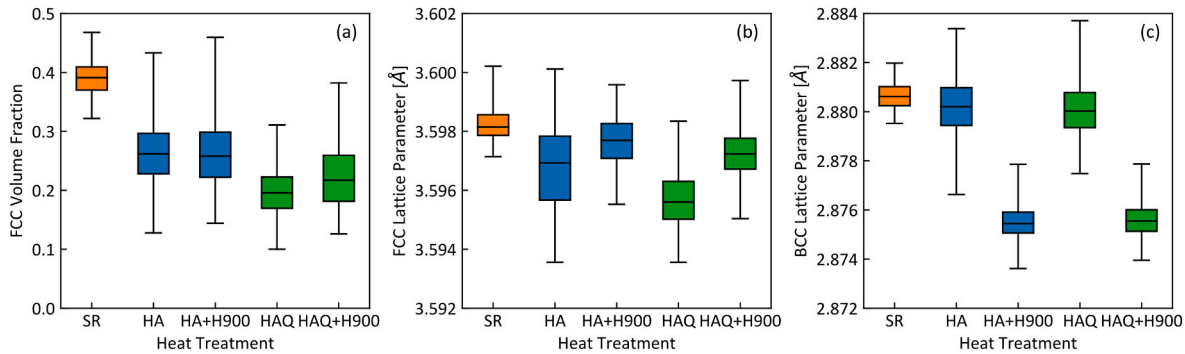

Fig. 5. Box plot of (a) FCC volume fraction, (b) FCC lattice parameter, and (c) BCC lattice parameter along the undeformed AM-SR, AM-HA, AM-HA+H900, AM-HAQ, and AM-HAQ+H900 tensile specimens. Each condition represents 100 data points measured 200 μm apart along the gauge of the undeformed specimens as shown in Fig. 1c and d.

Table 4
Average and standard deviation of FCC lattice parameter, BCC lattice parameter, and FCC volume fraction along undeformed tensile specimens for each material condition examined.

Heat Treatment	FCC Lattice Parameter	BCC Lattice Parameter	FCC Volume Fraction
	Å	Å	
AM-SR	3.5982 ± 0.0006	2.8806 ± 0.0005	0.390 ± 0.029
AM-HA	3.5968 ± 0.0016	2.8802 ± 0.0012	0.266 ± 0.062
AM-HA+H900	3.5977 ± 0.0009	2.8755 ± 0.0007	0.264 ± 0.059
AM-HAQ	3.5957 ± 0.0010	2.8802 ± 0.0012	0.198 ± 0.044
AM-HAQ+H900	3.5972 ± 0.0008	2.8756 ± 0.0007	0.224 ± 0.054

approximately 91% of the typical yield stress of wrought condition-A from Ref. [76]. This is the consequence of further austenite to martensite phase transformation during the liquid nitrogen treatment.

The H900 aging treatment (AM-HA+H900 and AM-HAQ+H900) altered the mechanical behavior as shown in Fig. 6c and d. The YS increased by more than 500 MPa and the UTS by 150 MPa compared to the unaged conditions, and the uniform elongation and fracture strain also increased. The AM-HAQ+H900 had a higher yield stress than AM-HA+H900 (1216 MPa versus 1075 MPa, respectively). Also, AM-HAQ+H900 meets the ASTM A693 [6] minimum requirement for wrought 17-4 SS with the H900 aging heat treatment (1170 MPa and 1310 MPa for the YS and UTS, respectively). The true stress at UTS for the AM-HA+H900 and AM-HAQ+H900 conditions are similar at ≈ 1690 MPa, as shown in Fig. 8b. The aging treatment on AM-SR (AM-SR+H900 condition) increased the YS, UTS and uniform elongation.

The local strain at fracture, as measured by DIC, is approximately the same for the AM-HA and AM-HA+H900 at ≈ 50% true effective strain, whereas the AM-HAQ and AM-HAQ+H900 conditions show ≈ 55% true effective strain at fracture (see Table 5). Note that the measured effective strains at fracture represent a lower limit on the true values due to the averaging that occurs in the DIC measurements. This is related to the resolution of the cameras, and that the exact fracture point can occur in-between frames. The challenges of measuring fracture initiation with DIC are reported in detail elsewhere [77]. The principal strain paths up to fracture for the different wrought and AM conditions are shown in Fig. 9. Local strains within the neck were not reported for AM-SR and AM-SR+H900 conditions due to atypical necking strain and cracks developing at or shortly after necking began, as shown in the DIC maps for AM-SR in Fig. 10a and b. Non-uniform deformation was expected for the AM-SR and AM-SR+H900 due to the heterogeneous AM microstructure. However, the other AM conditions also exhibited heterogeneous deformation along the gauge length, the degree of which varies with condition and specimen. For example, prior to uniform elongation, AM-HA+H900 specimen exhibits heterogeneous deformation as shown Fig. 10c at 0.10 m/m engineering strain. Furthermore, the localization behavior and neck strain distributions were not as uniform and symmetric as the wrought material (Fig. 10e).

Similar to many sheet materials, the wrought material localizes to a plane strain path (i.e., $\frac{\partial \varepsilon_2}{\partial t} \rightarrow 0$) due to the neck constraint as shown in Fig. 9a. Additionally, the Wr-H900 condition is more resistant to thinning, and it accommodates less through thickness ductility than the Wr-CondA (see **Section 3.4** for further analysis). However, the principal strain paths for the AM conditions indicate that the AM material does not accommodate localization in the thickness direction like the Wr-CondA and Wr-H900 conditions, and fracture occurs prior to any significant plane strain deformation on the surface, resulting in lower local ductility than the wrought conditions.

3.3. *Phase transformation behavior as a function of plastic strain*

The DIMT behaviors are shown as a function of von-Mises (VM) effective plastic strain for the different AM conditions in Fig. 11. The square and diamond symbols are the same interrupted experiments from Fig. 6, and circle data points are the failed specimens. The solid data points are the average and standard deviation of the data points measured within the gauge length of the sample for the undeformed and interrupted experiments. An average was not reported for the failed specimens because accumulated strains within the neck vary. In addition, the data reported for the failed specimens are affected by the triaxial stress state in the necked region, which will tend to accelerate the rate of DIMT [78,79]. Therefore, the FCC volume fraction data corresponding to the fractured specimens are an underestimation for strains after uniform elongation from Table 5 for uniaxial stress state. The austenite fraction as a function VM effective plastic strain was modeled using an exponential decay as:

$$f_\gamma = f_\gamma^\circ e^{-k\bar{\varepsilon}_p} \tag{2}$$

following [31,80,81], where f_γ° is the initial FCC volume fraction, $\bar{\varepsilon}_p$ is the VM effective plastic strain, and k is a constant associated with

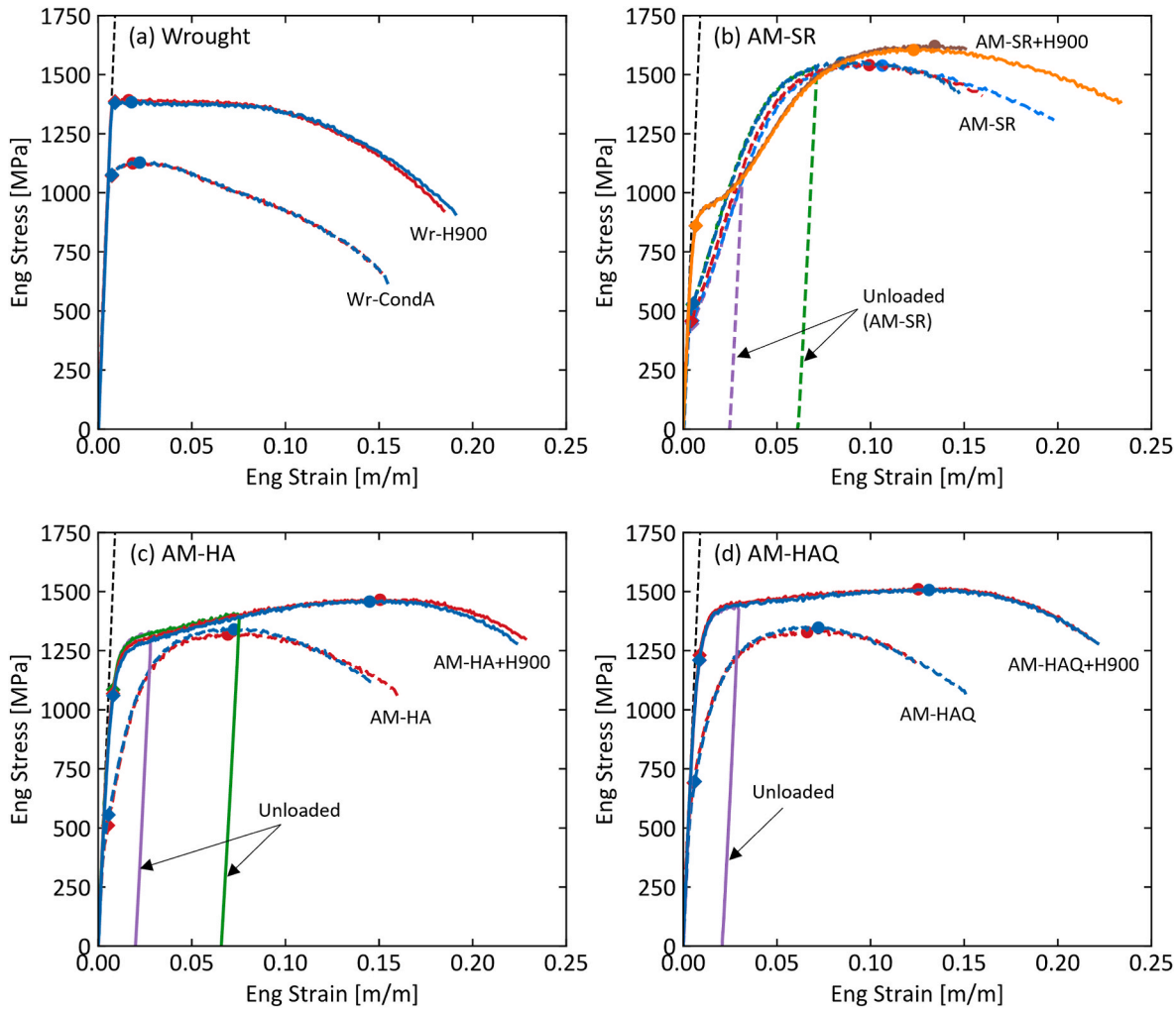

Fig. 6. Engineering (Eng) stress-strain curves for (a) Wr-CondA and Wr-H900, (b) AM-SR and AM-SR+H900, (c) AM-HA and AM-HA+H900, and (d) AM-HAQ and AM-HAQ+H900. The indicated unloaded curves are the interrupted experiments for the ex-situ HEXRD measurements in Fig. 11. All other experiments were loaded to failure, and they were repeated twice except for AM-SR condition which was repeated 3 times. The diamonds and circles represent the YS and UTS, respectively. The black dashed lines represent a 195 GPa elastic modulus. Note, one of the stress-strain curves in (d) for AM-HAQ condition failed prematurely due to a large internal flaw. Also, a different colors scheme in (b) for AM-SR+H900 was used due to the overlapping curves with AM-SR experiments. (For interpretation of the references to color in this figure legend, the reader is referred to the Web version of this article.)

mechanical stability of austenite, where k decreases as stability of austenite increases. The same k is used for AM-HA and AM-HAQ conditions, and for AM-HA+H900 and AM-HAQ+H900 conditions. The constants k for the different AM 17-4N conditions are presented in Table 6 and the results of the model are shown in Fig. 11.

For the AM-SR samples, the majority of the DIMT occurs within the first 5% $\bar{\varepsilon}_p$. The high transformation rate within the first few percent strain caused the high work hardening rate at low strains (see Fig. 8c). The rapid drop in the FCC phase fraction within the first 4% $\bar{\varepsilon}_p$ is consistent with the measurements reported by Phan *et al.* [45] on a similar AM 17-4N SS. For the AM-HA and AM-HAQ conditions (Fig. 11b and c), the austenite is less stable than the AM-SR condition, as the majority of the DIMT occurs within the first 3% $\bar{\varepsilon}_p$. However, for the aged material (AM-HA+H900 and AM-HAQ+H900), the mechanical stability of austenite increases, as the DIMT occurs more gradually over a larger range of plastic strain. For the AM-HAQ+H900, there is approximately no change in the FCC volume fraction within the first 2.2% $\bar{\varepsilon}_p$, but DIMT occurs rapidly thereafter.

3.4. Fracture surfaces

SEM images of the fracture surfaces from the different wrought and AM conditions are shown in Fig. 12. The wrought conditions neck more than the AM conditions, as shown in the first column in Fig. 12, and as reported for the local neck strain in **Section 3.2.2**. The average true local effective strain computed from the last DIC image prior to fracture for the wrought was ≈ 92% whereas the AM conditions was ≈ 52% (see Table 5). These results are consistent with Guennouni *et al.* [54], which showed a lower reduction in area at fracture for the AM 17-4 SS+H900 compared to wrought 17-4 SS + H900 condition. All samples examined exhibit ductile fracture, where micro-voids are present in the center of all the fracture surfaces examined. Many of the micro voids in the AM-HA and AM-HA+H900 conditions were likely formed at Nb-rich or Si + O rich precipitates as described in **Section 3.1**. The micro voids in the AM-SR are finer than the other AM and wrought conditions and are also located along dendritic-cellular features. The AM-SR condition exhibits local cleavage-like facets mainly about prior melt pool boundaries. Local cleavage-like facets are also present in the AM-HA and qualitatively more in the AM-HA+H900 condition, even though the local ductility is similar according to the DIC. The Wr-H900 sample exhibited large secondary cracks along the width of the fracture surface. This is likely a consequence of Wr-H900 resistance to thinning (as reported in **Section 3.2.2**), causing large stresses in the through-thickness direction at large strains [82].

Table 5
Average and standard deviation (± 1σ) of the elastic modulus (E), engineering 0.2% yield stress (YS), engineering ultimate tensile strength (UTS), engineering strain at UTS (uniform elongation), gauge length strain at fracture (fracture strain), local principal strains (ε_1 and ε_2) prior to fracture, and local effective strain ($\bar{\varepsilon}$) prior to fracture. The local DIC strains represent an average over a 0.5 mm diameter area in the center of the neck. See Section 2.5 for more information regarding ε_1, ε_2, and $\bar{\varepsilon}$. The average and standard deviation for E and YS contain the interrupted experiments while the other values are from the experiments loaded to failure. See Fig. 6 for exact number of experiments.

Material-Condition	E	YS	UTS	Uniform Elongation	Fracture Strain	ε_1	ε_2	$\bar{\varepsilon}$
	GPa	MPa	MPa	m/m	m/m	m/m	m/m	m/m
Wr-CondA	199 ± 1	1074 ± 3	1126 ± 2	0.020 ± 0.003	0.154 ± 0.001	0.959 ± 0.004	−0.323 ± 0.002	0.976 ± 0.005
Wr-H900	200 ± 2	1383 ± 5	1388 ± 6	0.017 ± 0.001	0.188 ± 0.003	0.864 ± 0.001	−0.342 ± 0.003	0.870 ± 0.001
AM-HA	153 ± 3	533 ± 32	1329 ± 16	0.071 ± 0.002	0.153 ± 0.006	0.471 ± 0.017	−0.220 ± 0.005	0.497 ± 0.021
AM-HAQ	167 ± 2	694 ± 4	1338 ± 13	0.069 ± 0.004	0.152 (1)	0.557 (1)	−0.272 (1)	0.557 (1)
AM-HA+H900	180 ± 1	1075 ± 13	1462 ± 5	0.148 ± 0.004	0.226 ± 0.002	0.490 ± 0.002	−0.232 ± 0.011	0.491 ± 0.002
AM-HAQ+H900	180 ± 1	1216 ± 12	1509 ± 2	0.128 ± 0.004	0.220 ± 0.001	0.545 ± 0.012	−0.270 ± 0.018	0.545 ± 0.011
AM-SR	175 ± 10	484 ± 42	1543 ± 7	0.097 ± 0.011	0.170 ± 0.021	n/a(2)	n/a(2)	n/a(2)
AM-SR+H900	185 ± 3	861 ± 1	1613 ± 12	0.129 ± 0.008	0.195 ± 0.045	n/a(2)	n/a(2)	n/a(2)

(1) One of the two experiments performed for this condition failed prematurely due to an internal flaw and therefore an average was not included for the fracture strain and the local strains.
(2) Local strains at fracture were not reported due to atypical neck strain as discussed in Section 3.2.2 and shown in Fig. 10a and Fig. 10b.

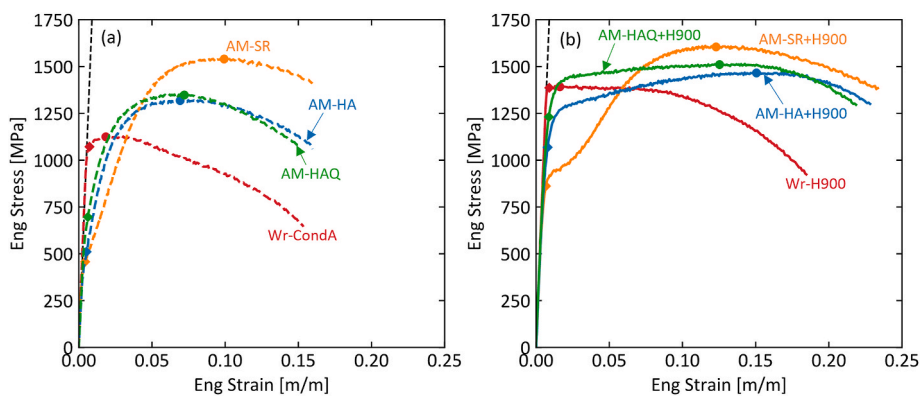

Fig. 7. A summary of engineering (Eng) stress-strain curves for (a) Wr-CondA, AM-SR, AM-HA, and AM-HAQ, and (b) Wr-H900, AM-SR+H900, AM-HA+H900, and AM-HAQ+H900. A representative stress-strain curve for each condition from Fig. 6 was used. The diamonds and circles represent the YS and UTS, respectively. The black dashed lines represent a 195 GPa elastic modulus.

3.5. Comparison with literature data

A comparison between the uniaxial tension data from this work with literature studies on wrought and AM 17-4 SS and 15-5 SS [22,46,47,52,54–61] is shown in Fig. 13. The figure compares uniform elongation versus YS in Fig. 13a and uniform elongation versus UTS in Fig. 13b. The same experiments are plotted for both subfigures, but with a different abscissa. Uniform elongation was chosen to represent the data because comparing the gauge length fracture strain can be misleading between samples having different gauge lengths. The uniform elongation is a better comparison between experiments as it should not vary significantly with different initial gauge lengths, and large uniform elongation is desirable for many structural applications. The vertical line in Figs. 13a and b represent the minimum YS and UTS requirements according to ASTM A693 and ASTM A564 for 17-4 SS in the H900 condition.

The dotted circled data groupings represent the present AM-SR condition and data from Shaffer *et al.* [22] on a similar AM material built from nitrogen-atomized 17-4 SS powder. That data group shows a low YS but high work hardening, leading to a high UTS, which is atypical for precipitation-hardenable martensitic stainless steels. The dashed circled data groupings represent typical behavior of wrought and AM 17-4 SS with H900 aging heat treatment. Within this grouping, which mimics most metals, as the YS increases, the hardening and the uniform strain typically decrease. However, the solid line circled grouping show a high combination of YS, UTS, and uniform elongation. The stars represent the AM-SR+H900, AM-HA + H900 and AM-HAQ + H900 conditions. The elongated diamond corresponds to the experimental data from Oh *et al.* [47], also on an AM 17-4 SS material built from nitrogen-atomized powder containing a mass fraction of 0.1% nitrogen in the powder composition. As such, retained stable austenite in the aged AM 17-4N SS can produce a material with strength and uniform ductility properties that are superior to the conventional 17-4 SS.

4. Discussion

4.1. Austenite stability

Martensitic steels are typically used for their high YS, but they exhibit poor hardening and low uniform elongation [83–85]. We have shown that retained austenite in AM 17-4N SS containing a mass fraction of 0.13% nitrogen can provide improved mechanical properties compared to wrought 17-4 SS and to AM 17-4 SS produced using argon-atomized and water-atomized feedstock powder (as shown in Section 3.5). In the AM-SR, AM-HA, and AM-HAQ conditions examined, the austenite was unstable and the majority of DIMT occurred within 5%

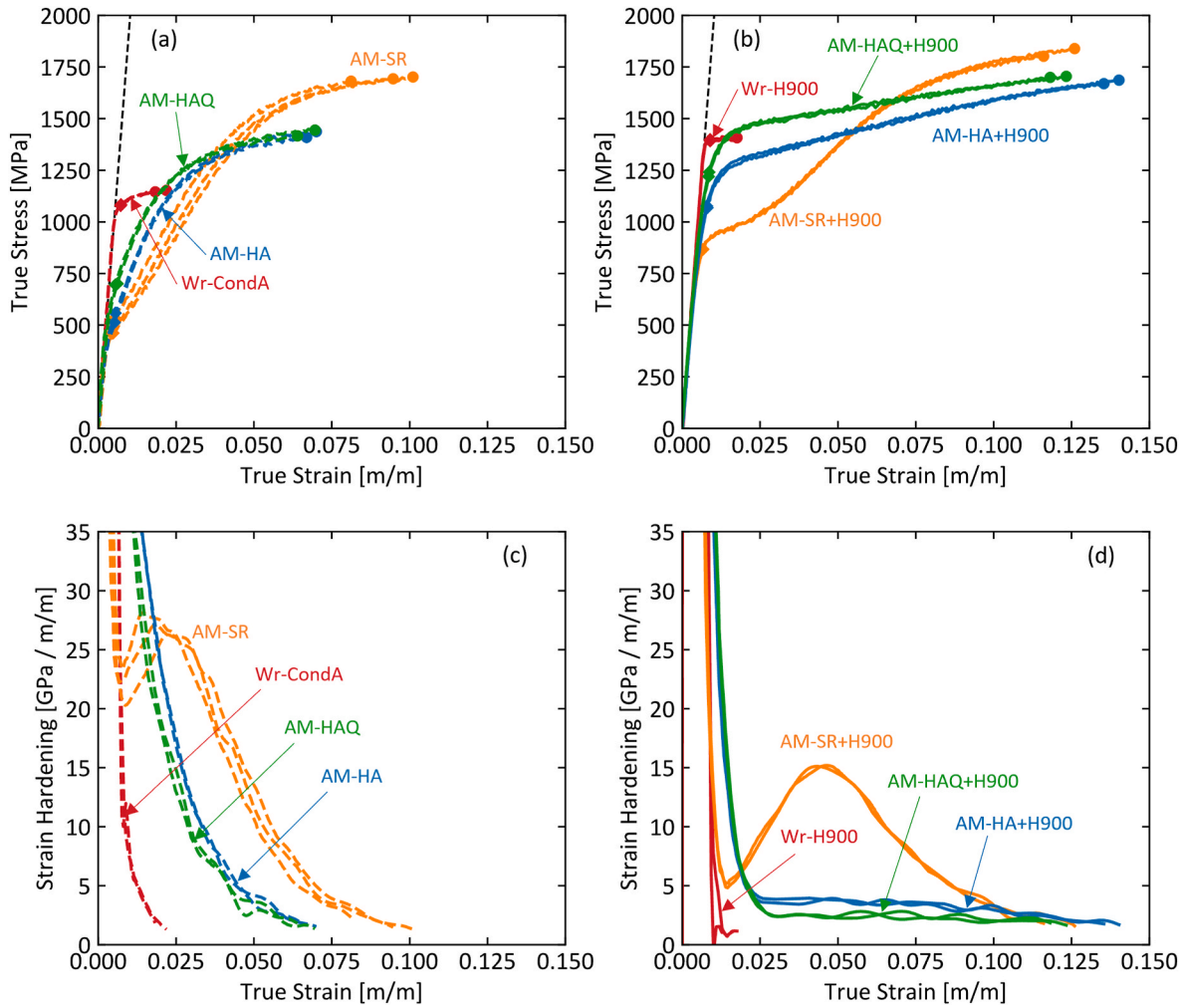

Fig. 8. True stress-strain curves up to UTS for (a) Wr-CondA, AM-SR, AM-HA, and AM-HAQ, and (b) for Wr-H900, AM-SR+H900, AM-HA+H900, and AM-HAQ+H900. The diamonds and circles in both (a) and (b) represent the true YS and UTS, respectively. The black dashed lines represent a 195 GPa elastic modulus. True strain hardening versus true strain up to UTS for (c) Wr-CondA, AM-SR, AM-HA, and AM-HAQ, and (d) for Wr-H900, AM-SR+H900, AM-HA+H900, and AM-HAQ+H900.

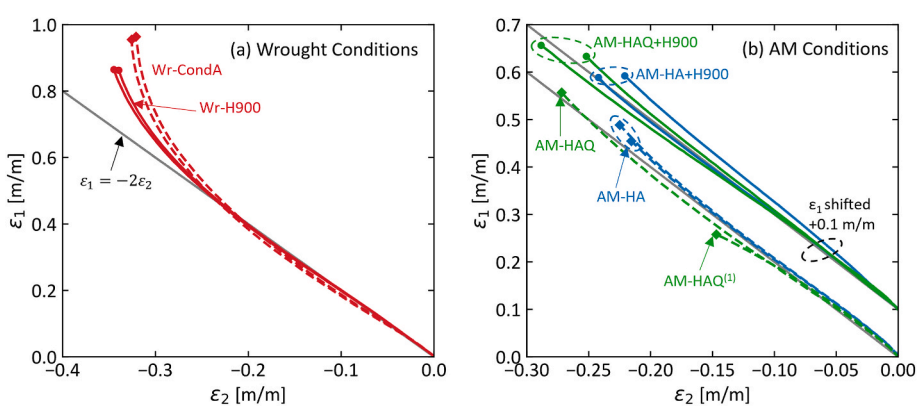

Fig. 9. Principal strain paths up to fracture for (a) Wr-CondA and Wr-H900, and (b) for AM-HA, AM-HA+H900, AM-HAQ, and AM-HAQ+H900 conditions. The DIC strains represent an average over a 0.5 mm diameter area in the center of the neck. (1)Experiment failed prematurely due to an internal flaw.

strain, resulting in steep work hardening at low plastic strains. However, after aging, the AM-HA+H900 and AM-HAQ+H900 conditions showed increased austenite stability, with the DIMT and strain hardening occurring over an extended range of plastic strain, resulting in an improved strength-hardening-ductility combination.

Elemental segregation or partitioning is an effective method that influences the austenite stability [43], which serves as the basis for Quenching and Partitioning (Q&P) processing of steel [35,86–88]. Partitioning occurs when austenite stabilizing elements diffuse from martensite towards retained austenite as each phase trends towards

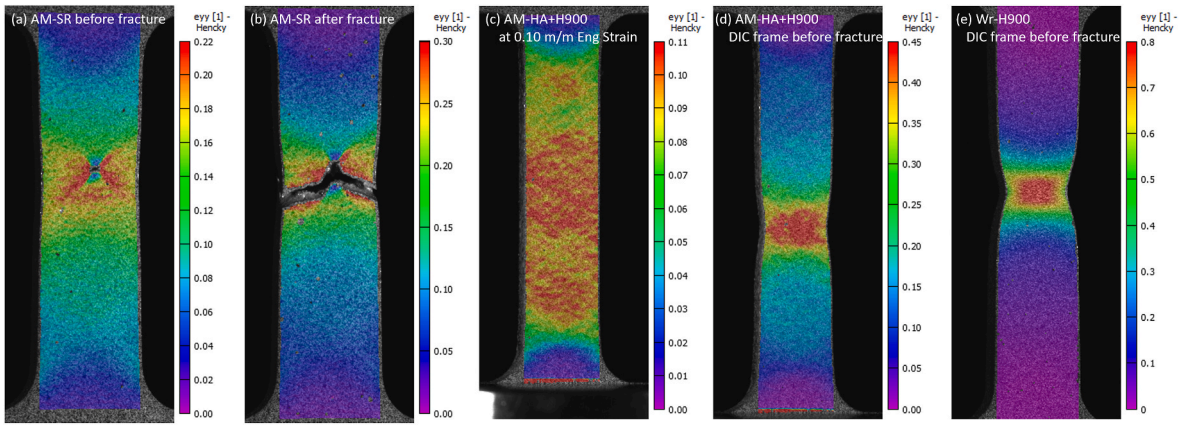

Fig. 10. High resolution DIC strain maps of Hencky ε_{yy} (true Hencky strain in the vertical direction) for (a) AM SR specimen a few DIC frames before fracture, (b) AM-SR specimen after fracture, (c) AM-HA+H900 specimen at 0.10 m/m engineering (Eng) strain, (d) AM-HA+H900 specimen the DIC frame before fracture, and (e) Wr-H900 specimen the DIC frame before fracture. Note, the DIC subset and step size was reduced to accentuate the crack and the heterogeneous deformation, but it also accentuates the noise and error.

Table 6
Model constant k (from Eq. (2)) for the different AM 17-4N conditions.

Condition	k
AM-SR	47.5
AM-HA	95.0
AM-HA+H900	11.8
AM-HAQ	95.0
AM-HAQ+H900	11.8

thermodynamic equilibrium. The heat treatment temperature determines the diffusivity of alloying elements, with interstitial elements segregating more quickly than substitutional elements at lower temperatures. For example, some steels utilize carbon diffusion to stabilize the austenite with short time at relatively low temperatures (e.g., 3 min at 450 °C [86]) to reduce the carbide formation. Similarly, the nitrogen in AM 17-4N SS can partition during aging at 482 °C, but it is difficult to quantify using the EDS maps at the measured length scale. However, elemental segregation into austenite typically leads to an increase in the FCC lattice parameter, which was reported earlier from the HEXRD measurements. The FCC lattice parameter (Å) can be calculated using the empirical relationship by Dyson-Homes [89].

$$\alpha_\gamma = 3.578 + 0.033C + 0.022N + 0.00095Mn - 0.0002Ni + 0.0006Cr + 0.0015Cu + 0.0031Mo + 0.0051Nb, \quad (3)$$

where the compositions are in mass fraction. As reported in Section 3.1, the FCC lattice parameter increased 0.0009 Å and 0.0015 Å once the AM-HA and AM-HAQ conditions were aged, respectively. This would require the diffusion of a mass fraction of 0.041% nitrogen and a mass fraction of 0.068% nitrogen into the FCC phase during aging for AM-HA and AM-HAQ conditions, respectively. The higher concentration of diffused nitrogen in the AM-HAQ+H900 condition would be expected since the martensite volume fraction was higher and therefore, higher mass fraction of nitrogen in solid solution within the martensite can diffuse into the austenite phase. The higher concentration of diffused elements for AM-HAQ+H900 compared to the AM-HA+H900 condition is consistent with our austenite stability results, where the austenite was more stable at low strains for the AM-HAQ+H900 condition. However, it is currently unknown why the FCC volume fraction in AM-HAQ+H900 decreases rapidly after 3% strain. This behavior could be a consequence of strain partitioning effects between the different phases and the strength properties of each phase of the AM-HAQ+H900 condition. Regardless, other austenite stabilizing elements, such as Ni and Mn can also have segregated during the aging process [10,90].

Residual stresses from the martensitic transformation can also alter the FCC lattice parameter. Hydrostatic stresses on the austenite phase induced from the shear and dilation of the martensitic transformation can decrease the FCC lattice parameter due to the elastic strains on the lattice [91–94]. These large stresses on the austenite phase can also stabilize the austenite at high volume fraction of martensite [91–95].

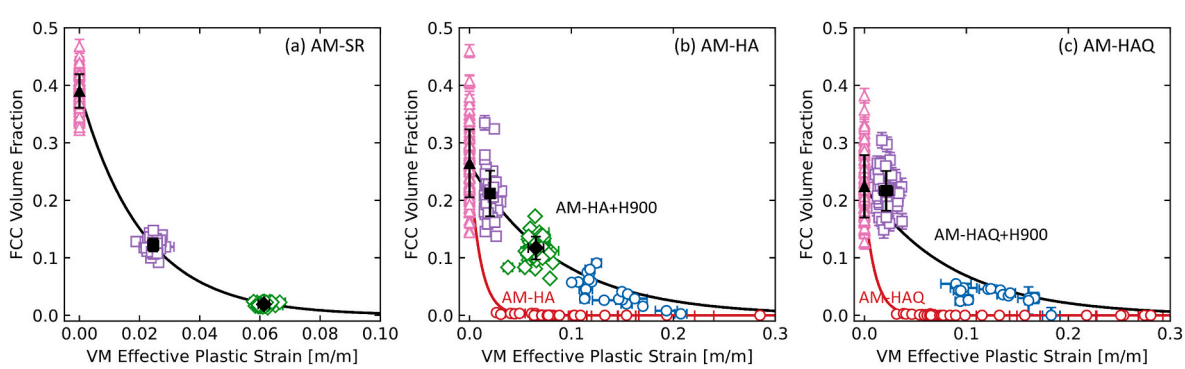

Fig. 11. FCC volume fraction as a function of von-Mises (VM) effective plastic strain determined by DIC measurements along the gauge length for (a) AM-SR, (b) AM-HA and AM-HA+H900, and (c) AM-HAQ and AM-HAQ+H900. The solid data points correspond to the average and one standard deviation of the set of data points for the undeformed (triangle symbols) and the interrupted experiments (square symbols and diamond symbols, see Fig. 6 for the interrupted stress-strain curves). The aged conditions were used to represent the undeformed data in (b) and (c). The circle data points in (b) and (c) are the failed specimens for the unaged and aged condition, respectively. Solid lines represent the model fits for Eq. (2).

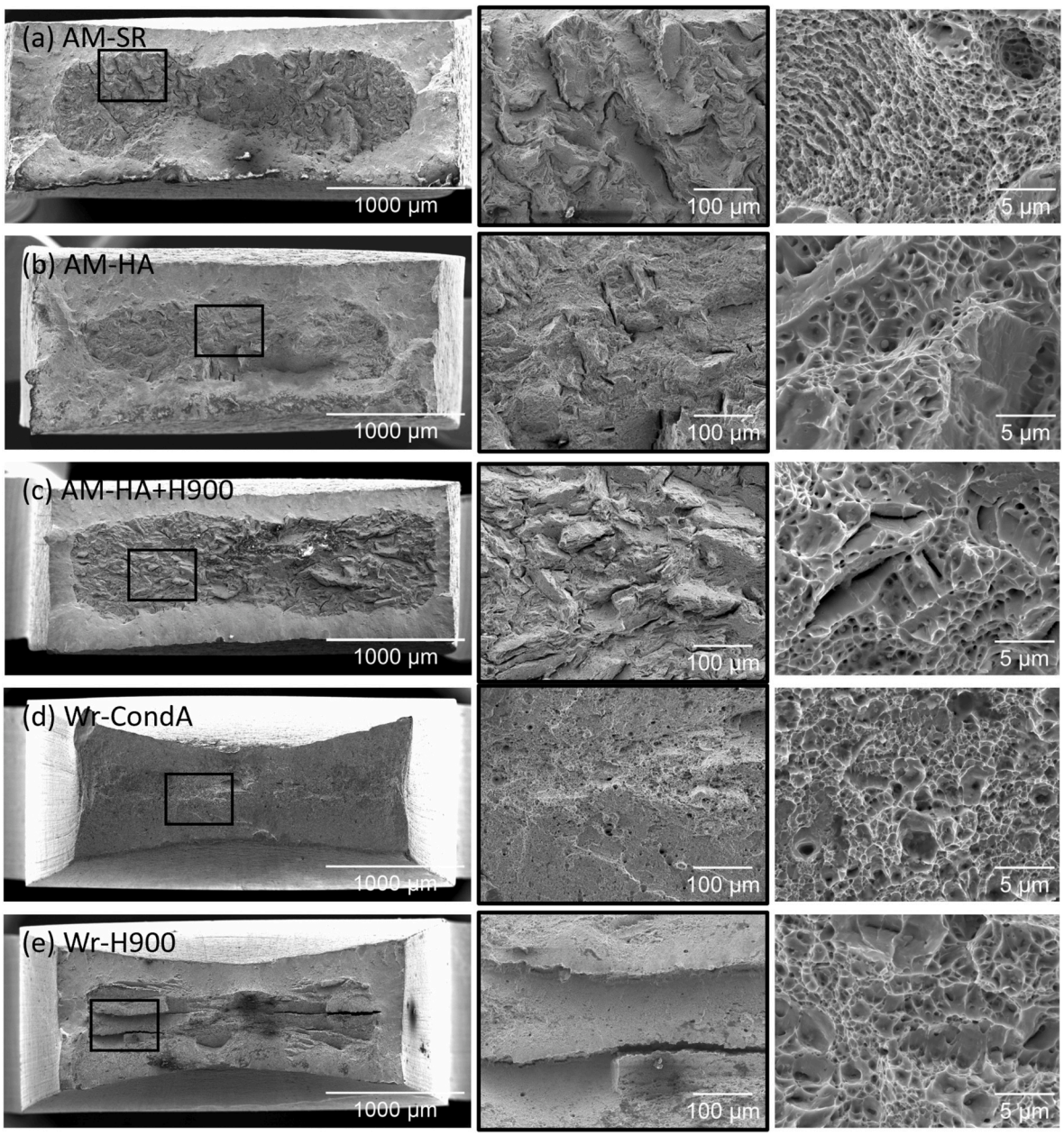

Fig. 12. SEM images of the fracture surfaces at different magnifications for the different conditions (a) AM-SR, (b) AM-HA, (c) AM-HA+H900 (d) Wr-CondA, and (e) Wr-H900.

However, the age-hardening process decreases the martensite lattice parameter due to Cu precipitation and elemental segregation. This process also relieves some hydrostatic stresses on the austenite which tends to increase the FCC lattice parameter. Therefore, both elemental segregation and stress relaxation can influence the FCC lattice parameter, making it difficult to conclude the exact mechanism(s) for the change in lattice parameters and improved austenite stability in aged AM 17-4N. Further examination with transmission electron microscopy (TEM), atomic probe tomography (APT), and/or modeling elemental segregation are needed to determine the reasons for the improved austenite stability.

4.2. Strengthening mechanisms

Various mechanisms influence the work hardening behavior of steels, DIMT being one of the most effective methods. Detailed explanations of the hardening mechanisms associated with DIMT are described elsewhere [31,32,91–97]. However, hardening associated with DIMT alone does not explain the high UTS of the AM material. A potential cause is the higher Cu content of the AM 17-4N SS which provides more precipitate strengthening potential [98], although both wrought and the AM compositions fall within the ASTM standard for 17-4 SS. It is important to note that the aging kinetics of Cu-rich precipitates in austenite is different than in martensite due to the solubility of Cu in austenite. Once the material is aged and deformed up to the UTS, the microstructure will consist of high strength tempered/aged martensite and likely lower strength fresh martensite transformed from DIMT that has yet to be tempered/aged. Therefore, the UTS of the aged AM 17-4N SS containing austenite should be less than that of aged 17-4N SS with no retained austenite if segregation within the austenite has not occurred. However, if nitrogen and/or other elements have segregated within the austenite during aging, the strength of the fresh martensite will be higher than without the addition of those elements. Nonetheless, other strengthening mechanisms will also influence the strength of the

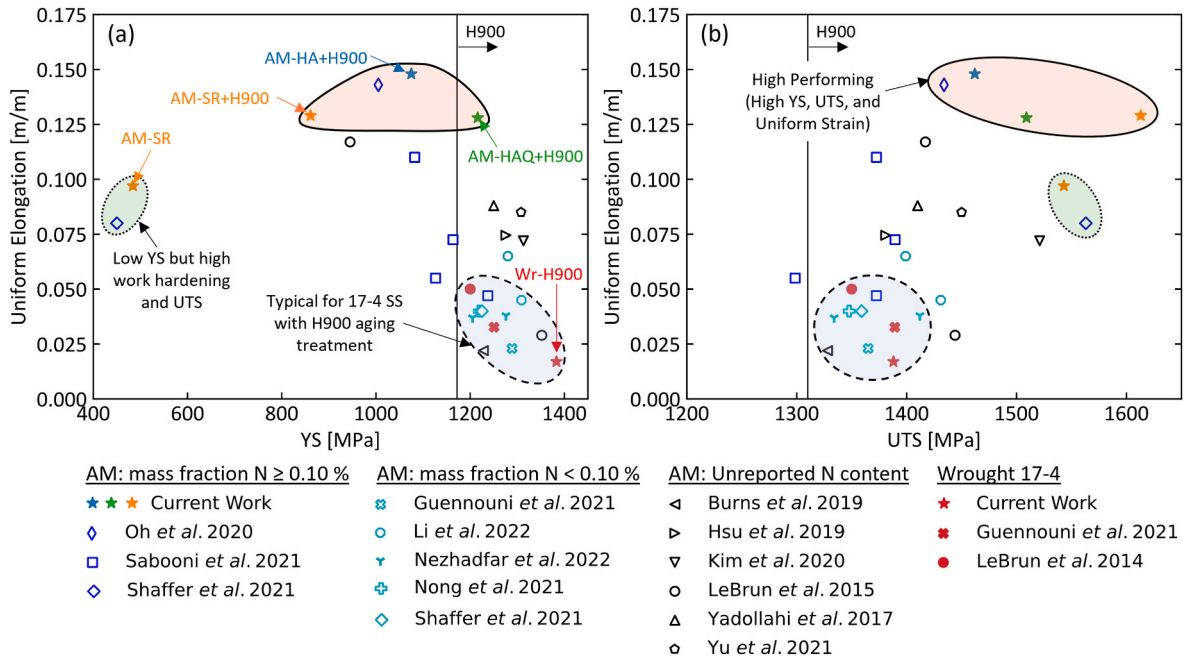

Fig. 13. Comparison between (a) uniform elongation versus YS and (b) uniform elongation versus UTS for different Wr 17-4 SS and AM 17-4 SS from the literature [22,46,47,52,54–63]. The star symbols are from this work and have the same color code as Fig. 7, and the other symbols are data from the literature. The vertical lines represent the minimum YS and UTS requirements for H900 according to ASTM A693 and ASTM A564. Data presented are for aged (H900 and H925) wrought and AM 17-4 SS and 15-5 SS only. If UE was not explicitly reported within the literature, the UE was estimated based on the stress-strain curve. Other conditions are not shown for simplicity. No comparison was made regarding loading orientation effects. Strain rates for the experiments reported within this figure are between ≈ 10^{-4} s^{-1} to 10^{-3} s^{-1}. (For interpretation of the references to color in this figure legend, the reader is referred to the Web version of this article.)

material at UTS, such as dislocation density variations with varying uniform elongation and solid solution strengthening, in addition to strengthening effects from Nb-rich and Si + O rich precipitates.

4.3. Uniform elongation versus local fracture ductility

The uniform elongations of the AM-HA+H900 and AM-HAQ+H900 conditions were higher than the Wr-H900 condition, as discussed in Section 3.2. The more stable austenite reduces the DIMT rate which assists in the hardening rate of the AM material and results in high uniform elongation. However, the local ductility in the neck region for the AM 17-4N SS conditions were lower than in the wrought 17-4 SS conditions. The lower local ductility of the AM material is due to multiple factors. One of the reasons is the volume fraction and size/distribution of the Nb-rich and Si + O rich precipitates formed during the HA heat treatment, which are crack nucleation sites. Furthermore, as mentioned in Section 3.4, many Nb-rich precipitates were adjacent to the Si + O rich precipitates, where the boundaries between the two are additional void nucleation sites for the AM material. Li *et al.* [62] also noticed similar NbC and oxide interfaces. They reported the shear modulus mismatch between the two precipitates can cause crack formation. The precipitates located along prior austenite grain boundaries (as shown in Section 3.1) are also detrimental to the local ductility of the material [99]. Finally, pores from the AM process are an additional source of reduced local ductility. Guo *et al.* [29] showed that an average of ≈ 50 nm diameter pores are present in their as-built AM 17-4. In summary, the reduced local ductility of the AM conditions, despite the improved work hardening behavior and uniform elongation from the retained austenite, is likely a combination of aforementioned mechanisms.

4.4. Processing of 17-4N SS

The post processing technique used for AM 17-4N SS is advantageous for AM parts, since it only requires a heat treatment to achieve the improvement in the work hardening behavior and ductility while maintaining high strength. While these improvements in the mechanical properties were reported in the AM 17-4N SS compared to wrought, it is expected that AM is not a necessary process to achieve such properties. The homogenization heat treatment eliminates the prior AM microstructure, leaving the properties dependent on the composition and microstructure after heat treatment. Similar to 316LN SS [25], nitrogen can be introduced into wrought 17-4 SS to achieve a large volume fraction of retained austenite at room temperature. An improvement in the mechanical properties compared to the AM 17-4N SS would be expected if Si–O rich precipitates are reduced, the grain structure is refined through thermo-mechanical processing, and if the composition is optimized. Furthermore, a sub-room temperature heat treatment would be unnecessary if the wrought material is cold worked, resulting in DIMT, to achieve the desired volume fraction of retained austenite prior to aging and stabilizing the austenite. However, many questions remain regarding the effect of DIMT in aged 17-4N SS on the corrosion properties, high temperature properties, strain rate properties, and fracture toughness.

5. Summary and conclusions

The influence of various heat treatments to alter the volume fraction and stability of the retained austenite, and on the resulting tensile behavior of AM 17-4 SS containing a mass fraction of 0.13% nitrogen (AM 17-4N SS) was investigated. This work led to the following conclusions:

1) Homogenization and austenization heat treatments resulted in an average austenite volume fraction of 0.27 at room temperature. The decrease in austenite fraction was attributed to the recrystallized microstructure and from the formation of nitrogen rich precipitates.

The subsequent liquid nitrogen treatment further decreased the average austenite volume fraction to 0.20.

2) In the unaged AM conditions, the austenite was unstable and the majority of the DIMT occurred in the first 5% plastic strain, which resulted in a low YS but high work hardening and high UTS. As such, the YS was approximately independent of the strength of the martensite when austenite was unstable and DIMT was the dominant deformation mechanism.
3) The H900 aging heat treatment maintained a relatively constant austenite fraction for both AM-HA and AM-HAQ conditions but increased the mechanical stability of austenite. The increase in austenite stability along with the precipitation hardening effect combined to increase the YS, UTS, and uniform elongation. The decrease in the DIMT rate caused a reduction in the hardening rate but distributed the hardening over a larger range of plastic strains, thereby increasing the uniform elongation. The increase in austenite stability was likely due to elemental segregation/partitioning from the martensite to the austenite phase during aging from nitrogen or from other stabilizing elements.
4) The local strains within the neck were lower for the AM conditions than the wrought conditions (≈ 51% versus ≈ 92%, respectively) despite the AM conditions having higher uniform elongation. The lower neck ductility in the AM conditions was attributed to the size/distribution of the Nb-rich and Si + O rich precipitates, and potentially from pores from the AM process.

Credit author statement

Saadi A. Habib: Conceptualization, Methodology, Formal analysis, Investigation, Writing – original draft, Visualization, Writing – review & editing. **Steven P. Mates**: Conceptualization, Formal analysis, Supervision, Writing – original draft, Writing – review & editing. **Fan Zhang**: Conceptualization, Formal analysis, Investigation, Writing – review & editing. **Mark R. Stoudt**: Formal analysis, Investigation, Writing – review & editing. **James S. Zuback**: Formal analysis, Investigation, Writing – review & editing. **Olaf Borkiewicz**: Formal analysis, Investigation, Writing – review & editing.

Declaration of competing interest

The authors declare that they have no known competing financial interests or personal relationships that could have appeared to influence the work reported in this paper.

Data availability

The raw/processed data required to reproduce these findings cannot be shared at this time as the data also forms part of an ongoing study.

Acknowledgements

We would like to thank Dr. Thien Phan, previously at NIST, for additively manufacturing the 17-4N SS material. We would also like to thank Dr. Kil-Won Moon from NIST for the encapsulation and the HA heat treatments of the AM samples. This research used resources of the Advanced Photon Source, a U.S. Department of Energy (DOE) Office of Science user facility operated for the DOE Office of Science by Argonne National Laboratory under Contract No. DE-AC02-06CH11357.

References

[1] A.K. Steel, 17–4 PH Stainless Steel Bulletin, 2016.
[2] P.J. Othen, M.L. Jenkins, G.D.W. Smith, W.J. Phythian, Transmission electron microscope investigations of the structure of copper precipitates in thermally-aged Fe—Cu and Fe—Cu—Ni, Phil. Mag. Lett. 64 (1991) 383–391.
[3] P.J. Othen, M.L. Jenkins, G.D.W. Smith, High-resolution electron microscopy studies of the structure of Cu precipitates in α-Fe, Philos. Mag. A 70 (1994) 1–24.
[4] T.-H. Lee, Y.-O. Kim, S.-J. Kim, Crystallographic model for bcc-to-9R martensitic transformation of Cu precipitates in ferritic steel, Phil. Mag. 87 (2007) 209–224.
[5] Y.-U. Heo, Y.-K. Kim, J.-S. Kim, J.-K. Kim, Phase transformation of Cu precipitates from bcc to fcc in Fe–3Si–2Cu alloy, Acta Mater. 61 (2013) 519–528.
[6] ASTM A693, Specification for Precipitation-Hardening Stainless and Heat-Resisting Steel Plate, Sheet, and Strip, ASTM International, 2016.
[7] H.A. Hardouin Duparc, R.C. Doole, M.L. Jenkins, A. Barbu, A high-resolution electron microscopy study of copper precipitation in Fe-1.5 wt% Cu under electron irradiation, Phil. Mag. Lett. 71 (1995) 325–333.
[8] T. Zhou, R. Prasath Babu, J. Odqvist, H. Yu, P. Hedström, Quantitative electron microscopy and physically based modelling of Cu precipitation in precipitation-hardening martensitic stainless steel 15-5 PH, Mater. Des. 143 (2018) 141–149.
[9] L. Couturier, F. De Geuser, M. Descoins, A. Deschamps, Evolution of the microstructure of a 15-5PH martensitic stainless steel during precipitation hardening heat treatment, Mater. Des. 107 (2016) 416–425.
[10] T. Zhou, B. Neding, S. Lin, J.-C. Tseng, P. Hedström, Cu precipitation-mediated formation of reverted austenite during ageing of a 15–5 PH stainless steel, Scripta Mater. 202 (2021), 114007.
[11] R. Bhambroo, S. Roychowdhury, V. Kain, V.S. Raja, Effect of reverted austenite on mechanical properties of precipitation hardenable 17-4 stainlesssteel, Mater. Sci. Eng., A 568 (2013) 127–133.
[12] S.D. Dobson, T.L. Starr, Powder characterization and part density for powder bed fusion of 17-4 PH stainless steel, Rapid Prototyp. J. 27 (2020) 53–58.
[13] G.M. Janowski, F.S. Biancaniello, S.D. Ridder, Beneficial effects of nitrogen atomization on an austenitic stainless steel, MTA 23 (1992) 3263–3272.
[14] J.S. Weaver, J. Whiting, V. Tondare, C. Beauchamp, M. Peltz, J. Tarr, T.Q. Phan, M. A. Donmez, The effects of particle size distribution on the rheological properties of the powder and the mechanical properties of additively manufactured 17-4 PH stainless steel, Addit. Manuf. 39 (2021), 101851.
[15] M.R. Stoudt, R.E. Ricker, E.A. Lass, L.E. Levine, Influence of postbuild microstructure on the electrochemical behavior of additively manufactured 17-4 PH stainless steel, JOM 69 (2017) 506–515.
[16] M.R. Stoudt, C.E. Campbell, R.E. Ricker, Examining the relationship between post-build microstructure and the corrosion resistance of additively manufactured 17-4PH stainless steel, Materialia 22 (2022), 101435.
[17] W. DeLong, A modified phase diagram for stainless steel weld metals, Metal Progress 77 (1960) 99–100B.
[18] A. Schaeffler, Welding dissimilar metals with stainless electrodes, Iron Age 162 (1948) 72–79.
[19] L.E. Murr, E. Martinez, J. Hernandez, S. Collins, K.N. Amato, S.M. Gaytan, P. W. Shindo, Microstructures and properties of 17-4 PH stainless steel fabricated by selective laser melting, J. Mater. Res. Technol. 1 (2012) 167–177.
[20] H.K. Rafi, D. Pal, N. Patil, T.L. Starr, B.E. Stucker, Microstructure and mechanical behavior of 17-4 precipitation hardenable steel processed by selective laser melting, J. Mater. Eng. Perform. 23 (2014) 4421–4428.
[21] L. Facchini, N. Vicente, I. Lonardelli, E. Magalini, P. Robotti, A. Molinari, Metastable austenite in 17-4 precipitation-hardening stainless steel produced by selective laser melting, Adv. Eng. Mater. 12 (2010) 184–188.
[22] D.J. Shaffer, A.E. Wilson-Heid, J.S. Keist, A.M. Beese, T.A. Palmer, Impact of retained austenite on the aging response of additively manufactured 17-4 PH grade stainless steel, Mater. Sci. Eng. 817 (2021), 141363.
[23] W.E. Luecke, J.A. Slotwinski, Mechanical properties of austenitic stainless steel made by additive manufacturing, J. Res. Natl. Inst. Stan. 119 (2014) 398.
[24] F. Zhang, M.R. Stoudt, S. Hammadi, C.E. Campbell, E.A. Lass, M.E. Williams, How austenitic is a martensitic steel produced by laser powder bed fusion? A Cautionary Tale, Metals. 11 (2021) 1924.
[25] ASTM A276, Specification for Stainless Steel Bars and Shapes, ASTM International, 2017.
[26] AMS5355J, Aerospace Material Specification, Steel, Corrosion Resistant, Investment Castings 16Cr-4.1Ni-0.28Cb-3.2Cu-Homogenization and Solution Heat Treated or Homogenization, Solution, and Precipitation Heat Treated, 2015.
[27] E.A. Lass, M.R. Stoudt, M.E. Williams, Additively manufactured nitrogen-atomized 17-4 PH stainless steel with mechanical properties comparable to wrought, Metall. Mater. Trans. 50 (2019) 1619–1624.
[28] S. Cheruvathur, E.A. Lass, C.E. Campbell, Additive manufacturing of 17-4 PH stainless steel: post-processing heat treatment to achieve uniform reproducible microstructure, JOM 68 (2016) 930–942.
[29] Q. Guo, M. Qu, C.A. Chuang, L. Xiong, A. Nabaa, Z.A. Young, Y. Ren, P. Kenesei, F. Zhang, L. Chen, Phase Transformation Dynamics Guided Alloy Development for Additive Manufacturing, Additive Manufacturing, 2022, 103068.
[30] S.D. Meredith, J.S. Zuback, J.S. Keist, T.A. Palmer, Impact of composition on the heat treatment response of additively manufactured 17–4 PH grade stainless steel, Mater. Sci. Eng., A 738 (2018) 44–56.
[31] G.B. Olson, M. Cohen, Kinetics of strain-induced martensitic nucleation, MTA 6 (1975) 791–795.
[32] D. Fahr, Stress- and strain-induced formation of martensite and its effects on strength and ductility of metastable austenitic stainless steels, Metall. Mater. Trans. B 2 (1971) 1883–1892.
[33] V.F. Zackay, E.R. Parker, Treatment of Steel, US3488231A, 1970.
[34] V.F. Zackay, E.R. Parker, D. Fahr, R. Busch, The enhancement of ductility in high-strength steels, ASM Trans. Quart. 60 (1967) 252–259.
[35] J.G. Speer, F.C.R. Assunção, D.K. Matlock, D.V. Edmonds, The "quenching and partitioning" process: background and recent progress, Mater. Res. 8 (2005) 417–423.
[36] J. Speer, D.K. Matlock, B.C. De Cooman, J.G. Schroth, Carbon partitioning into austenite after martensite transformation, Acta Mater. 51 (2003) 2611–2622.

[37] C.B. Finfrock, B. Ellyson, S.R.J. Likith, D. Smith, C.J. Rietema, A.I. Saville, M. M. Thrun, C.G. Becker, A.L. Araujo, E.J. Pavlina, J. Hu, J.-S. Park, A.J. Clarke, K. D. Clarke, Elucidating the temperature dependence of TRIP in Q&P steels using synchrotron X-Ray diffraction, constituent phase properties, and strain-based kinetics models, Acta Mater. 237 (2022), 118126.
[38] R.L. Miller, Ultrafine-grained Microstructures and Mechanical Properties of Alloy Steels, 1972, pp. 905–912. MT. 3.
[39] J. Talonen, H. Hänninen, Formation of shear bands and strain-induced martensite during plastic deformation of metastable austenitic stainless steels, Acta Mater. 55 (2007) 6108–6118.
[40] T. Angel, Formation of martensite in austenitic stainless steels, J. Iron Steel Inst 177 (1954) 165–174.
[41] S.S. Hecker, M.G. Stout, K.P. Staudhammer, J.L. Smith, Effects of strain state and strain rate on deformation-induced transformation in 304 stainless steel: Part I. Magnetic measurements and mechanical behavior, MTA 13 (1982) 619–626.
[42] L.E. Murr, K.P. Staudhammer, S.S. Hecker, Effects of strain state and strain rate on deformation-induced transformation in 304 stainless steel: Part II. Microstructural study, MTA 13 (1982) 627–635.
[43] B. He, On the factors governing austenite stability: intrinsic versus extrinsic, Materials 13 (2020) 3440.
[44] W.A. Poling, Tensile Deformation of Third Generation Advanced High Strength Sheet Steels under High Strain Rates, Colorado School of Mines, 2016. Ph.D. dissertation.
[45] T.Q. Phan, F.H. Kim, D.C. Pagan, Micromechanical response quantification using high-energy X-rays during phase transformations in additively manufactured 17-4 stainless steel, Mater. Sci. Eng., A 759 (2019) 565–573.
[46] T. LeBrun, T. Nakamoto, K. Horikawa, H. Kobayashi, Effect of retained austenite on subsequent thermal processing and resultant mechanical properties of selective laser melted 17–4 PH stainless steel, Mater. Des. 81 (2015) 44–53.
[47] W. Oh, Solution annealing and precipitation hardening effect on the mechanical properties of 630 stainless steel fabricated via laser melting deposition, Mater. Sci. (2020) 23.
[48] E.A. Lass, F. Zhang, C.E. Campbell, Nitrogen effects in additively manufactured martensitic stainless steels: conventional thermal processing and comparison with wrought, Metall. Mater. Trans. 51 (2020) 2318–2332.
[49] S.F. Siddiqui, A.A. Fasoro, C. Cole, A.P. Gordon, Mechanical characterization and modeling of direct metal laser sintered stainless steel GP1, J. Eng. Mater. Technol. 141 (2019), 031009.
[50] S. Mates, M. Stoudt, G. Jacob, W. Moscoso, V. Madhavan, Dynamic thermal softening behavior of additive materials for hybrid manufacturing, in: Mechanics of Additive and Advanced Manufacturing, 8, Springer, 2019, pp. 31–34.
[51] T.L. Starr, K. Rafi, B. Stucker, C.M. Scherzer, Controlling phase composition in selective laser melted stainless steeels, in: 2012 International Solid Freeform Fabrication Symposium, 2012, p. 8.
[52] D.E. Burns, A. Kudzal, B. McWilliams, J. Manjarres, D. Hedges, P.A. Parker, Investigating additively manufactured 17-4 PH for structural applications, J. Mater. Eng. Perform. 28 (2019) 4943–4951.
[53] A. Kudzal, B. McWilliams, C. Hofmeister, F. Kellogg, J. Yu, J. Taggart-Scarff, J. Liang, Effect of scan pattern on the microstructure and mechanical properties of Powder Bed Fusion additive manufactured 17-4 stainless steel, Mater. Des. 133 (2017) 205–215.
[54] N. Guennouni, A. Barroux, C. Grosjean, D. Maisonnette, E. Nivet, E. Andrieu, D. Poquillon, L. Laffont, C. Blanc, Comparative study of the microstructure between a laser beam melted 17-4PH stainless steel and its conventional counterpart, Mater. Sci. Eng. 823 (2021), 141718.
[55] T. Lebrun, K. Tanigaki, K. Horikawa, H. Kobayashi, Strain rate sensitivity and mechanical anisotropy of selective laser melted 17-4 PH stainless steel, Mech. Eng. J. 1 (2014) SMM0049. SMM0049.
[56] S.H. Kim, S.-M. Yeon, J.H. Lee, Y.W. Kim, H. Lee, J. Park, N.-K. Lee, J.P. Choi, C. Aranas, Y.J. Lee, S. An, K. Choi, Y. Son, Additive manufacturing of a shift block via laser powder bed fusion: the simultaneous utilisation of optimised topology and a lattice structure, Virtual Phys. Prototyp. 15 (2020) 460–480.
[57] A. Yadollahi, N. Shamsaei, S.M. Thompson, A. Elwany, L. Bian, Effects of building orientation and heat treatment on fatigue behavior of selective laser melted 17-4 PH stainless steel, Int. J. Fatig. 94 (2017) 218–235.
[58] T.-H. Hsu, Y.-J. Chang, C.-Y. Huang, H.-W. Yen, C.-P. Chen, K.-K. Jen, A.-C. Yeh, Microstructure and property of a selective laser melting process induced oxide dispersion strengthened 17-4 PH stainless steel, J. Alloys Compd. 803 (2019) 30–41.
[59] S. Sabooni, A. Chabok, S.C. Feng, H. Blaauw, T.C. Pijper, H.J. Yang, Y.T. Pei, Laser powder bed fusion of 17–4 PH stainless steel: a comparative study on the effect of heat treatment on the microstructure evolution and mechanical properties, Addit. Manuf. 46 (2021), 102176.
[60] X.D. Nong, X.L. Zhou, Y.D. Wang, L. Yu, J.H. Li, Effects of geometry, location, and direction on microstructure and mechanical properties of 15–5PH stainless steel fabricated by directed energy deposition, Mater. Sci. Eng. 821 (2021), 141587.
[61] Z. Yu, Z. Chai, J. Xu, J. Chen, J. Chen, C. Yu, H. Lu, Achieving high strength and ductility in 17-4 PH steel with a periodic layer structure by laser direct metal depositing and aging, Mater. Sci. Eng. 824 (2021), 141787.
[62] K. Li, J. Zhan, T. Yang, A.C. To, S. Tan, Q. Tang, H. Cao, L.E. Murr, Homogenization timing effect on microstructure and precipitation strengthening of 17–4PH stainless steel fabricated by laser powder bed fusion, Addit. Manuf. 52 (2022), 102672.
[63] P.D. Nezhadfar, P.R. Gradl, S. Shao, N. Shamsaei, Microstructure and deformation behavior of additively manufactured 17–4 stainless steel: laser powder bed fusion vs. Laser powder directed energy deposition, JOM 74 (2022) 1136–1148.
[64] ASTM A564, Specification for Hot-Rolled and Cold-Finished Age-Hardening Stainless Steel Bars and Shapes, ASTM International, 2019.
[65] C. Rowolt, B. Milkereit, P. Andreazza, O. Kessler, Quantitative high temperature calorimetry on precipitation in steel and nickel alloys, Thermochimica Acta 677 (2019) 169–179.
[66] ASTM A747, Standard Specification for Steel Castings, Stainless, Precipitation Hardening, 2020.
[67] F. Bachmann, R. Hielscher, H. Schaeben, Texture analysis with MTEX–free and open source software toolbox, in: Solid State Phenomena, Trans Tech Publ, 2010, pp. 63–68.
[68] ASTM E92, Test Methods for Vickers Hardness and Knoop Hardness of Metallic Materials, ASTM International, 2017.
[69] E. Jones, M. Iadicola, R. Bigger, B. Blaysat, C. Boo, M. Grewer, J. Hu, A. Jones, M. Klein, K. Raghavan, P. Reu, T. Schmidt, T. Siebert, M. Simenson, D. Turner, A. Vieira, T. Weikert, A Good Practices Guide for Digital Image Correlation, first ed., International Digital Image Correlation Society, 2018.
[70] E.8 ASTM, Test Methods for Tension Testing of Metallic Materials, ASTM International, 2021.
[71] Z. Liang, I. Zhirnov, F. Zhang, K.K. Jones, D. Deisenroth, M. Williams, U. Kattner, K. Moon, W.-K. Liu, B. Lane, C. Campbell, Development of computational framework for titanium alloy phase transformation prediction in laser powder-bed fusion additive manufacturing, Materialia 14 (2020), 100934.
[72] Steel AMS5604J, Corrosion Resistant, Sheet, Strip, and Plate 16.5Cr - 4.0Ni - 4.0Cu - 0.30Cb Solution Heat Treated, Precipitation Hardenable, 2018.
[73] E. Turdogan, Fundamentals of Steelmaking, The Institute of Materials, 1996.
[74] A. Creuziger, C.A. Calhoun, W.A. Poling, T. Gnäupel-Herold, Assessment of bias errors caused by texture and sampling methods in diffraction-based steel phase measurements, J. Appl. Crystallogr. 51 (2018) 720–731.
[75] A. Creuziger, T. Phan, D. Pagan, Refinements in phase fraction determination of textured alloys from transmission diffraction data, J. Appl. Crystallogr. 54 (2021) 1480–1489.
[76] ATI, 17-4 PH Technical Data Sheet, 2016.
[77] S.A. Habib, J.T. Lloyd, C.S. Meredith, A.S. Khan, S.E. Schoenfeld, Fracture of an anisotropic rare-earth-containing magnesium alloy (ZEK100) at different stress states and strain rates: experiments and modeling, Int. J. Plast. 122 (2019) 285–318.
[78] P. Jacques, Q.F. Mont, T. Pardoen, F. Delannay, On the role of martensitic transformation on damage and cracking resistance in trip-assisted multiphase steels, Acta Mater. 49 (2001) 139–152.
[79] R.G. Stringfellow, D.M. Parks, G.B. Olson, A constitutive model for transformation plasticity accompanying strain-induced martensitic transformations in metastable austenitic steels, Acta Metall. Mater. 40 (1992) 1703–1716.
[80] K. Sugimoto, N. Usui, M. Kobayashi, S. Hashimoto, Effects of volume fraction and stability of retained austenite on ductility of TRIP-aided dual-phase steels, ISIJ Int. 32 (1992) 1311–1318.
[81] K.-I. Sugimoto, M. Kobayashi, S.-I. Hashimoto, Ductility and strain-induced transformation in a high-strength transformation-induced plasticity-aided dual-phase steel, Metall. Mater. Trans. A 23 (1992) 3085–3091.
[82] F. Zok, J.D. Embury, On the analysis of delamination fractures in high-strength steels, MTA 21 (1990) 2565–2575.
[83] S.A. Habib, C.S. Meredith, A.S. Khan, Quasi-static and dynamic investigation of an advanced high strength and corrosion resistant 10 % Cr nanocomposite martensitic steel, Int. J. Mech. Sci. 211 (2021), 106774.
[84] H.J. Rack, Physical and Mechanical Properties of Cast 17-4 PH Stainless Steel, 1981.
[85] G. Krauss, Quench and tempered martensitic steels, in: Comprehensive Materials Processing, Elsevier, 2014, pp. 363–378.
[86] J. Mola, B.C. De Cooman, Quenching and partitioning (Q&P) processing of martensitic stainless steels, Metall. Mater. Trans. 44 (2013) 946–967.
[87] J. Mola, B.C. De Cooman, Quenching and partitioning processing of transformable ferritic stainless steels, Scripta Mater. 65 (2011) 834–837.
[88] M. Wendler, C. Ullrich, M. Hauser, L. Krüger, O. Volkova, A. Weiß, J. Mola, Quenching and partitioning (Q&P) processing of fully austenitic stainless steels, Acta Mater. 133 (2017) 346–355.
[89] D. Dyson, B. Holmes, Effect of alloying additions on the lattice parameter of austenite, J. Iron Steel Inst. 208 (1970) 469–474.
[90] O. Dmitrieva, D. Ponge, G. Inden, J. Millán, P. Choi, J. Sietsma, D. Raabe, Chemical gradients across phase boundaries between martensite and austenite in steel studied by atom probe tomography and simulation, Acta Mater. 59 (2011) 364–374.
[91] N. Nakada, Y. Ishibashi, T. Tsuchiyama, S. Takaki, Self-stabilization of untransformed austenite by hydrostatic pressure via martensitic transformation, Acta Mater. 110 (2016) 95–102.
[92] M. Hayakawa, M. Oka, On the change in the austenite lattice parameter due to the martensitic transformation in an Fe-32Ni alloy, Acta Metall. 31 (1983) 955–959.
[93] Y. Tanaka, K. Shimizu, Anomalous changes in austenite and martensite lattice parameters of Fe-Mn-C alloys, Trans. JIM. 21 (1980) 42–50.
[94] K. Golovchiner, Changes in the austenite lattice parameter during the martensitic transformation in steel, Phys. Met. Metallogr. 37 (1974) 126–130.
[95] J.R. Patel, M. Cohen, Criterion for the action of applied stress in the martensitic transformation, Acta Metall. 1 (1953) 531–538.
[96] B.P.J. Sandvik, C.M. Wayman, Characteristics of lath martensite: Part I. crystallographic and substructural features, MTA 14 (1983) 809–822.

[97] F. Maresca, V.G. Kouznetsova, M.G.D. Geers, On the role of interlath retained austenite in the deformation of lath martensite, Model. Simulat. Mater. Sci. Eng. 22 (2014), 045011.
[98] S. Wang, K. Yang, M. Shen, C. Yang, Effect of Cu Content on Antibacterial Activity of 17-4 PH Stainless Steel, (n.d.)..
[99] H.R. Habibi Bajguirani, The effect of ageing upon the microstructure and mechanical properties of type 15-5 PH stainless steel, Mater. Sci. Eng., A 338 (2002) 142–159.